Monthly Notices
of the
ROYAL ASTRONOMICAL SOCIETY

MNRAS **464,** 4045–4062 (2017)
Advance Access publication 2016 October 5

doi:10.1093/mnras/stw2464

Cosmology from large-scale galaxy clustering and galaxy–galaxy lensing with Dark Energy Survey Science Verification data

J. Kwan,[1⋆] C. Sánchez,[2] J. Clampitt,[1] J. Blazek,[3] M. Crocce,[4] B. Jain,[1] J. Zuntz,[5] A. Amara,[6] M. R. Becker,[7,8] G. M. Bernstein,[1] C. Bonnett,[2] J. DeRose,[7,8] S. Dodelson,[9,10,11] T. F. Eifler,[12] E. Gaztanaga,[4] T. Giannantonio,[13,14] D. Gruen,[8,15†] W. G. Hartley,[16] T. Kacprzak,[16] D. Kirk,[17] E. Krause,[8] N. MacCrann,[5] R. Miquel,[2,18] Y. Park,[19] A. J. Ross,[3] E. Rozo,[19] E. S. Rykoff,[8,15] E. Sheldon,[20] M. A. Troxel,[5] R. H. Wechsler,[7,8,15] T. M. C. Abbott,[21] F. B. Abdalla,[17,22] S. Allam,[9] A. Benoit-Lévy,[23,17,24] D. Brooks,[17] D. L. Burke,[8,15] A. Carnero Rosell,[25,26] M. Carrasco Kind,[27,28] C. E. Cunha,[8] C. B. D'Andrea,[29,30] L. N. da Costa,[25,26] S. Desai,[32,31] H. T. Diehl,[9] J. P. Dietrich,[32,31] P. Doel,[17] A. E. Evrard,[33,34] E. Fernandez,[2] D. A. Finley,[9] B. Flaugher,[9] P. Fosalba,[2] J. Frieman,[9,10] D. W. Gerdes,[34] R. A. Gruendl,[27,28] G. Gutierrez,[9] K. Honscheid,[3,35] D. J. James,[21] M. Jarvis,[1] K. Kuehn,[36] O. Lahav,[17] M. Lima,[37,25] M. A. G. Maia,[25,26] J. L. Marshall,[38] P. Martini,[3,39] P. Melchior,[40] J. J. Mohr,[32,31,41] R. C. Nichol,[29] B. Nord,[9] A. A. Plazas,[12] K. Reil,[15] A. K. Romer,[42] A. Roodman,[8,15] E. Sanchez,[43] V. Scarpine,[9] I. Sevilla-Noarbe,[43] R. C. Smith,[21] M. Soares-Santos,[9] F. Sobreira,[44,25] E. Suchyta,[1,45] M. E. C. Swanson,[28] G. Tarle,[34] D. Thomas,[29] V. Vikram,[46] A. R. Walker[21] and The DES Collaboration

Affiliations are listed at the end of the paper

Accepted 2016 September 28. Received 2016 September 24; in original form 2016 April 26; Editorial Decision 2016 September 26

ABSTRACT

We present cosmological constraints from the Dark Energy Survey (DES) using a combined analysis of angular clustering of red galaxies and their cross-correlation with weak gravitational lensing of background galaxies. We use a 139 deg^2 contiguous patch of DES data from the Science Verification (SV) period of observations. Using large-scale measurements, we constrain the matter density of the Universe as $\Omega_{\rm m} = 0.31 \pm 0.09$ and the clustering amplitude of the matter power spectrum as $\sigma_8 = 0.74 \pm 0.13$ after marginalizing over seven nuisance parameters and three additional cosmological parameters. This translates into $S_8 \equiv \sigma_8(\Omega_{\rm m}/0.3)^{0.16} = 0.74 \pm 0.12$ for our fiducial lens redshift bin at $0.35 < z < 0.5$, while $S_8 = 0.78 \pm 0.09$ using two bins over the range $0.2 < z < 0.5$. We study the robustness of the results under changes in the data vectors, modelling and systematics treatment, including photometric redshift and shear calibration uncertainties, and find consistency in the derived cosmological parameters. We show that our results are consistent with previous cosmological analyses from DES and other data sets and conclude with a joint analysis of DES angular clustering and galaxy–galaxy lensing with *Planck* Cosmic Microwave Background data, baryon accoustic oscillations and Supernova Type Ia measurements.

Key words: gravitational lensing: weak – cosmological parameters – large-scale structure of Universe.

⋆ E-mail: kjuliana@physics.upenn.edu
† Einstein fellow.

1 INTRODUCTION

Since the discovery of cosmic acceleration, the nature of dark energy has emerged as one of the most important open problems in cosmology. Wide-field, large-volume galaxy surveys are promising avenues to answer cosmological questions, since they provide multiple probes of cosmology, such as baryon acoustic oscillations (BAOs), large-scale structure, weak lensing and cluster counts from a single data set. Moreover, some of these probes can be combined for greater effect, since each is sensitive to their own combination of cosmological parameters and systematic effects. In this paper, we will focus on combining the large-scale angular clustering of galaxies with measurements of the gravitational lensing produced by the large-scale structure traced by the same galaxies, as observed in the Dark Energy Survey (DES).

Measurements of the large-scale clustering of galaxies are among the most mature probes of cosmology. The positions of galaxies are seeded by the distribution of dark matter on large scales and the manner in which the growth of structure proceeds from gravitational collapse is sensitive to the relative amounts of dark matter and energy in the Universe. There is a long history of using large-volume galaxy surveys for the purposes of constraining cosmology, including DES, Sloan Digital Sky Survey (SDSS; York et al. 2000), Hyper Suprime-Cam (HSC; Miyazaki et al., 2012), the Kilo-Degree Survey (KiDS; de Jong et al. 2013; de Jong et al. 2015; Kuijken et al. 2015), and the Canada France Hawaii Telescope Lensing Survey (CFHTLenS; Heymans et al. 2012; Erben et al. 2013).

Gravitational lensing, the deflection of light rays by massive structures, provides a complementary method of probing the matter distribution. Here, we focus on galaxy–galaxy lensing (Tyson, Valdes & Mills 1984; Brainerd, Blandford & Smail 1996), when both the lenses and sources are galaxies. This involves correlating the amount of distortion in the shapes of background galaxies with the positions of foreground galaxies. The amount of distortion is indicative of the strength of the gravitational potential along the line of sight and therefore tells us about the amount of matter contained in the lens plane. Weak gravitational lensing produces two effects, magnification of the source and shearing of its image, but this analysis is only concerned with the latter. These have been used to probe both cosmology (Cacciato et al. 2013; Mandelbaum et al. 2013; More et al. 2015) and the structure of dark matter haloes and its connection to the galaxy distribution and baryon content of the Universe (Sheldon et al. 2004; Mandelbaum et al. 2006; Mandelbaum, Seljak & Hirata 2008; Cacciato et al. 2009; Leauthaud et al. 2012; Gillis et al. 2013; Velander et al. 2014; Hudson et al. 2015; Sifón et al. 2015; Viola et al. 2015; van Uitert et al. 2016).

Individual studies of large-scale structure (Crocce et al. 2016), galaxy–galaxy lensing (Clampitt et al. 2016) and cosmic shear (Becker et al. 2016; The Dark Energy Survey Collaboration et al. 2016a) using DES data as well as combined analyses focusing on smaller scales (Park et al. 2016) have been presented elsewhere. In this paper, we combine angular clustering and galaxy–galaxy lensing to jointly estimate the large-scale galaxy bias and matter clustering and constrain cosmological parameters.

The plan of the paper is as follows. Section 2 outlines the theoretical framework for modelling the angular galaxy correlation function and galaxy–galaxy lensing. Section 3 describes the galaxy sample used and the measurements from DES data, as well as the covariance between the two probes. Our cosmology results are summarized in Section 4 including constraints on a five-parameter ΛCDM (Lambda cold dark matter) model and a six-parameter *w*CDM model, where *w*, the dark energy equation-of-state parameter is also allowed to vary. We discuss the robustness of our results and our tests for systematic errors in Section 5. Finally, we combine our analysis with other probes of cosmology and compare our results to previous results in the literature in Section 6. Our conclusions are presented in Section 7.

2 THEORY

We are interested in describing the angular clustering of galaxies, $w(\theta)$, and the tangential shear produced by their host dark matter haloes, $\gamma_t(\theta)$, as a function of cosmology. The angular correlation function, $w(\theta)$, can be expressed in terms of the galaxy power spectrum as:

$$C(\ell) = \frac{1}{c}\int d\chi \left(\frac{n_l(\chi)H(\chi)}{\chi}\right)^2 P_{\rm gg}(\ell/\chi), \quad (1)$$

$$w(\theta) = \int \frac{\ell d\ell}{2\pi} C(\ell) J_0(\ell\theta), \quad (2)$$

where $P_{\rm gg}$ is the galaxy auto power spectrum, J_0 is the Bessel function of order 0, l is the angular wavenumber, χ is the comoving radial coordinate, $H(\chi)$ is the Hubble relation, c is the speed of light, and $n_l(\chi)$ is the number of galaxies as a function of radial distance from the observer, normalized such that $\int_{\chi_{\rm min}}^{\chi_{\rm max}} n_l(\chi)\,{\rm d}\chi = 1$. Note that equation (2) uses the Limber approximation (Limber 1953; Kaiser 1992), such that the radial distribution of galaxies, $n_l(\chi)$, is assumed to be slowly varying over our redshift slice. We have also ignored the contribution of redshift-space distortions to the angular clustering; this is expected to be small due to the width of the redshift intervals used; for the full expression, see Crocce et al. (2016).

The tangential shear is given by:

$$\langle\gamma_t(\theta)\rangle = 6\pi\Omega_{\rm m}\int {\rm d}\chi\, n_l(\chi)\frac{f(\chi)}{a(\chi)}\int {\rm d}k\, k P_{g\delta}(k,\chi)J_2(k,\theta,\chi), \quad (3)$$

where $f(\chi) = \int {\rm d}\chi' n_{\rm s}(\chi')\chi(\chi-\chi')/\chi'$ is the lens efficiency, a is the scale factor and $n_l(\chi)$, and $n_{\rm s}(\chi)$ are the selection functions of the lenses (foreground) and source (background) galaxies, respectively. The foreground galaxies supply the gravitational potentials that lens the background galaxies. The tangential shear is a measurement of the amount of distortion introduced into the images of background galaxies from the gravitational potentials along the line of sight as a function of scale. We will discuss the impact of photometric redshift (photo-z) errors on the lens and source distributions and propagate these to the measured cosmological constraints in Section 5.

The combination of these two probes has been extensively discussed in the literature (Baldauf et al. 2010; Yoo & Seljak 2012; Mandelbaum et al. 2013; Park et al. 2016) and provide another means by which we can mine the rich, well-calibrated DES-Science Verification (SV) data set. Unlike Park et al. (2016), we restrict our modelling to sufficiently large scales such that we are not sensitive to how galaxies populate individual haloes, i.e. halo occupation distribution (HOD) modelling is unnecessary. On these scales, we are only concerned with correlations between galaxies that reside in different haloes (the 2-halo term of the power spectrum), and we can relate the matter power spectrum, $P_{\delta\delta}$, to the galaxy power spectrum, $P_{\rm gg}$, and galaxy–dark matter cross-power spectrum, $P_{g\delta}$, via the following relationships:

$$P_{\rm gg}(k) \approx b_{\rm g}^2 P_{\delta\delta}(k), \quad (4)$$

$$P_{g\delta}(k) \approx b_{\rm g} r P_{\delta\delta}(k), \quad (5)$$

where b_g is the linear bias that relates the clustering of galaxies to that of dark matter and r is the cross-correlation coefficient that captures the stochasticity between the clustering of dark matter and the clustering of galaxies; see for example Seljak (2000) and Guzik & Seljak (2001).

The measurement of $w(\theta)$ depends on $b_g^2 P_{\delta\delta}$, while the tangential shear, $\gamma_t(\theta)$, depends on $b_g P_{\delta\delta}$ if $r = 1$, a reasonable approximation on the large scales we use in this work (we allow for and marginalize over possible stochasticity through our nonlinear bias modelling; see Section 2.1). The measurements of $w(\theta)$ and $\gamma_t(\theta)$ in combination allow us to estimate both the clustering amplitude and the linear galaxy bias, thus enabling us to obtain useful cosmological information.

2.1 Nonlinear bias model

The assumption of linear bias in equations (4) and (5) is expected to break down at small scales. In order to account for this effect, we use the nonlinear biasing scheme of McDonald (2006), where the galaxy overdensity, δ_g, is written as follows:

$$\delta_g = \epsilon + b_1\delta + b_2\delta^2 + \text{next leading order bias terms}, \quad (6)$$

where b_1 is the usual linear bias, b_2 is the next leading order bias term and ϵ is the shot noise. The bias parameters, b_1 and b_2 are not known a priori and become free parameters to be constrained during the analysis. Under this perturbation theory scheme, the galaxy–dark matter and galaxy–galaxy power spectra become

$$P_{g\delta} = b_1 P_{\delta\delta} + b_2 A(k), \quad (7)$$

$$P_{gg} = b_1^2 P_{\delta\delta} + b_1 b_2 A(k) + b_2 B(k) + N, \quad (8)$$

where N is the shot noise and $A(k)$ and $B(k)$ can be calculated using standard perturbation theory as follows:

$$A(k) = \int \frac{d^3q}{(2\pi)^3} F_2(\mathbf{q}, \mathbf{k}-\mathbf{q}) P_{\delta\delta}(q) P_{\delta\delta}(|\mathbf{k}-\mathbf{q}|), \quad (9)$$

$$B(k) = \int \frac{d^3q}{(2\pi)^3} P_{\delta\delta}(q) P_{\delta\delta}(|\mathbf{k}-\mathbf{q}|), \quad (10)$$

where $F_2(\mathbf{k_1}, \mathbf{k_2}) = \frac{5}{7}\frac{(\mathbf{k_1}+\mathbf{k_2})\cdot\mathbf{k_2}}{k_1^2} + \frac{1}{7}(\mathbf{k_1}+\mathbf{k_2})^2 \frac{\mathbf{k_1}\cdot\mathbf{k_2}}{k_1^2 k_2^2}$. Note that this nonlinear biasing scheme generates departures from $r = 1$ as $r \approx 1 - 1/4(b_2/b_1)^2 \xi_{gg}$, where ξ_{gg} is the correlation function. As such we do not include an additional free parameter for the cross-correlation coefficient. We found that for reasonable values of the shot noise, N, given the density of our galaxy sample, has a less than 5 per cent effect on $w(\theta)$ on scales below our regime of interest (<20 arcmin) and so have ignored this term for the remainder of our analysis. We do, however, include an additional additive constant term in configuration space as discussed in Section 5. This term mainly alters the large-scale clustering to allow for possible systematics coming from observational effects (see Section 5.6).

We investigate the inclusion of the next order biasing term in Section 5.1, in which we vary both the lower limit on the angular scale cutoff and the modelling of nonlinear bias.

3 DATA AND MEASUREMENTS

The DES is an ongoing photometric survey that aims to cover 5000 deg^2 of the Southern sky in five photometric filters, *grizY*, to a depth of $i \sim 24$ over a five-year observational programme using the Dark Energy Camera (DECam; Flaugher et al. 2015) on the 4 m Blanco Telescope at the Cerro Tololo Inter-American Observatory (CTIO) in Chile. In this analysis, we will be utilizing DES-SV data, in particular a contiguous ∼139 deg^2 patch known as the SPT-E region (because of its overlap with the South Pole Telescope survey footprint). This is only a small (∼3 per cent) subset of the expected eventual sky coverage of DES, but observations in all five filters have been performed at full depth, although substantial depth variations are present [see e.g. Leistedt et al. (2016)], mainly due to weather and early DECam operational challenges. The DES-SV data have been used for constraining cosmology in this work, but a rich variety of science cases are possible with this data sample [see The Dark Energy Survey Collaboration et al. (2016b) and references therein].

The lens galaxy sample used in this work is a subset of the DES-SV galaxies selected by redMaGiC[1] (Rozo et al. 2016), which is an algorithm designed to define a sample of the luminous red galaxies (LRGs) by minimizing the photo-z uncertainty associated with the sample. It selects galaxies based on how well they fit a red-sequence template, as described by their goodness-of-fit, χ^2. The red-sequence template is calibrated using REDMAPPER (Rykoff et al. 2014; Rozo et al. 2015) and a subset of galaxies with spectroscopically verified redshifts. The cutoff in the goodness-of-fit, $\chi^2_{\rm cut}$, is imposed as a function of redshift and adjusted such that a constant comoving number density of galaxies is maintained, since red galaxies are expected to be passively evolving. The redMaGiC photo-z's show excellent performance, with a median photo-z bias, $(z_{\rm spec} - z_{\rm phot})$, of 0.005 and scatter, $\sigma_z/(1+z)$, of 0.017. Equally important, their errors are very well characterized, enabling the redshift distribution of a sample, $N(z)$, to be determined by stacking each galaxy's Gaussian redshift probability distribution function [see Rozo et al. (2016) for more details].

The galaxy shape catalogues used in this work were presented in Jarvis et al. (2016), and they have been used in several previous analyses (Becker et al. 2016; Gruen et al. 2016; The Dark Energy Survey Collaboration et al. 2016a; Vikram et al. 2015; Clampitt et al. 2016). Two different catalogues exist corresponding to the NGMIX[2] (Sheldon 2014) and IM3SHAPE[3] (Zuntz et al. 2013) shear pipelines, both producing model-fitting shape measurements to a subset of the DES-SV galaxies. The two catalogues differ in their approach to modelling the intrinsic galaxy shape (NGMIX uses a Gaussian mixture model to approximate an exponential disc galaxy profile while IM3SHAPE determines the maximum likelihood for fitting a bulge and/or disc profile) and also in the number of filters used (NGMIX uses *riz* bands while IM3SHAPE only uses *r* band). This results in the NGMIX catalogue containing more sources than IM3SHAPE (∼6.9 galaxies per arcmin^2 versus ∼4.2 galaxies per arcmin^2). More details about the pipelines and an extensive set of null and systematics tests can be found in Jarvis et al. (2016). The photo-z distributions of the galaxies in the shear catalogues were studied in detail in Bonnett et al. (2016), using four different photo-z codes that performed well in a previous more extensive photo-z code comparison (Sánchez et al. 2014). The four methods are SKYNET (Graff et al. 2014; Bonnett et al. 2016), ANNZ2 (Sadeh, Abdalla & Lahav 2016), TPZ (Carrasco Kind & Brunner 2013) and BPZ (Benítez 2000). The first three methods are training-based, and the last is a widely used template-based code. Details about their training or calibration

[1] https://des.ncsa.illinois.edu/releases/sva1
[2] https://github.com/esheldon/ngmix
[3] https://bitbucket.org/joezuntz/im3shape

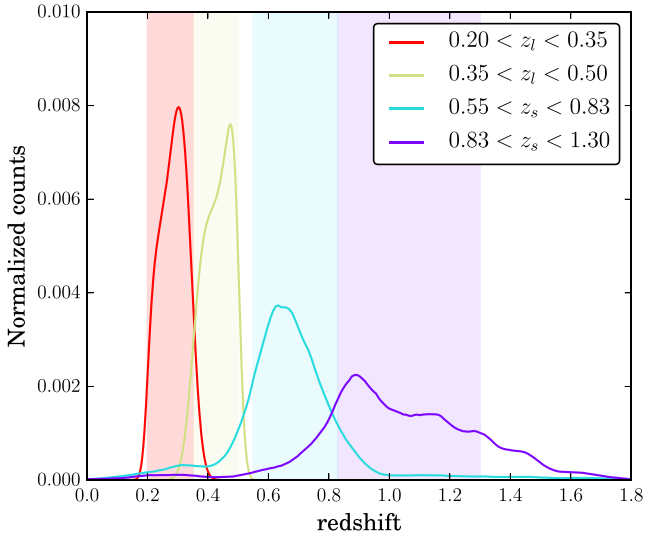

Figure 1. Redshift distributions of the four galaxy samples used in this work. Red and yellow curves correspond to the two redMaGiC lens bins while cyan and purple curves correspond to the two source bins in the fiducial configuration (NGMIX shears, SKYNET photo-z's).

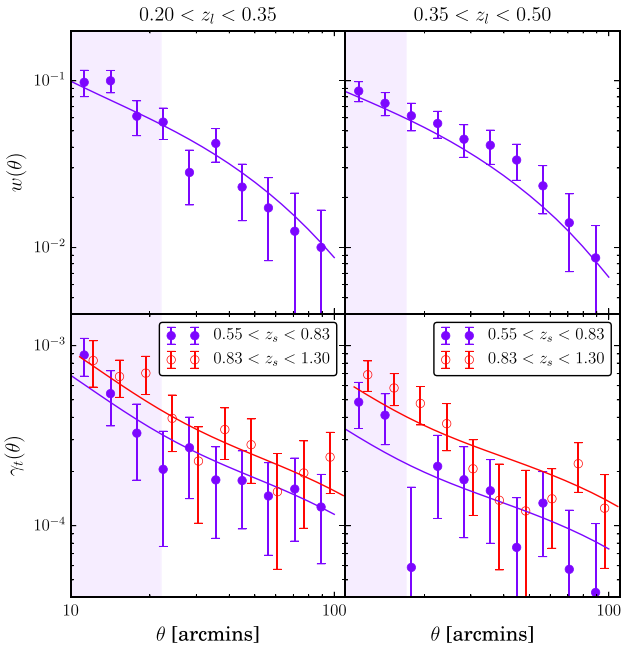

Figure 2. Angular galaxy clustering and galaxy–galaxy lensing measurements used in this work. For the two-lens bins (left- and right-hand columns), we show the clustering measurements (upper row) and the galaxy–galaxy lensing measurements (lower row) for the two source bins, with error bars coming from jackknife resampling. The shaded region shows excluded scales in the fiducial analysis, explored in Section 5.1. The predictions for the best-fitting curves presented in Section 4 are shown as the solid curves in each panel. The goodness-of-fit, as measured by the χ^2 value is 6 (3.5) for 12 (9) degrees of freedom for the high-z (low-z) bin. While these reduced χ^2 values seem low, there is no evidence that the errors are overestimated to within 2σ.

procedures and about the validation against spectroscopic data can be found in Bonnett et al. (2016).

In this paper, we use the NGMIX shear catalogue and SKYNET photo-z's for the fiducial results, but we will test the robustness of our results with the IM3SHAPE shear catalogue as well as using the source distributions derived from the other photo-z algorithms in the analysis.

3.1 Measurements

We use two-lens bins, selected using redMaGiC photo-z's: $0.20 < z < 0.35$ and $0.35 < z < 0.50$, and two source bins, selected using SKYNET photo-z's: $0.55 < z < 0.83$ and $0.83 < z < 1.30$. The same lens photo-z bins are analysed in Clampitt et al. (2016) while the source photo-z bins are studied in detail in Bonnett et al. (2016) and used for cosmology in The Dark Energy Survey Collaboration et al. (2016a). Individual analyses involving $\gamma_t(\theta)$ and $w(\theta)$ with DES-SV have been presented in Clampitt et al. (2016) and Crocce et al. (2016), respectively. Fig. 1 shows the redshift distributions for the lens and source bins utilized in this analysis. For each lens bin, we measure the galaxy clustering and the galaxy–galaxy lensing signals using the estimators defined next. The correlation functions have been estimated using the code TREECORR[4] (Jarvis, Bernstein & Jain 2004).

3.1.1 *Angular clustering – w(θ)*

On the galaxy clustering side, we compute the angular correlation function for each redshift bin using the minimum variance estimator of Landy & Szalay (1993),

$$w(\theta) = \frac{\mathrm{DD} - 2\mathrm{DR} + \mathrm{RR}}{\mathrm{RR}}, \tag{11}$$

where θ is the angular separation in the sky, and DD, DR and RR are data–data, data–random and random–random pairs of galaxies, with data and random galaxies having the exact same geometry in the sky. For the random catalogues, we use 136 185 random points ($\sim$7 and $\sim$15 times the number of galaxies in the fiducial bin and low-z bin, respectively) and apply the same angular masking as the redMaGiC galaxies in the SV region. The resulting measurement is shown in Fig. 2. The clustering amplitude falls from $\sim 10^{-1}$ to 10^{-2} over the range $\theta = 10 - 100$ arcmin. Only scales $\sim$20 arcmin and above will be used in the cosmology fits (see Section 5.1 for details). The details of the calculation of the error or covariance matrix for $w(\theta)$ will be presented in Section 3.2.

3.1.2 *Tangential shear – $\gamma_t(\theta)$*

On the lensing side, the observable is the tangential shear, i.e. the shear of the source galaxy which is perpendicular to the projected line joining the lens and source galaxies. For a given lens–source pair (j) this is given by

$$\gamma_{t,j} = -\gamma_{1,j}\cos(2\phi_j) - \gamma_{2,j}\sin(2\phi_j), \tag{12}$$

where $\gamma_{1,j}$ and $\gamma_{2,j}$ are the two components of shear measured with respect to a Cartesian coordinate system with origin in the lens galaxy, and ϕ_j is the position angle of the source galaxy with respect to the horizontal axis of the Cartesian coordinate system. Since the intrinsic ellipticity of individual source galaxies is much larger than the weak-lensing shear, it is necessary to average over many such

[4] https://github.com/rmjarvis/TreeCorr

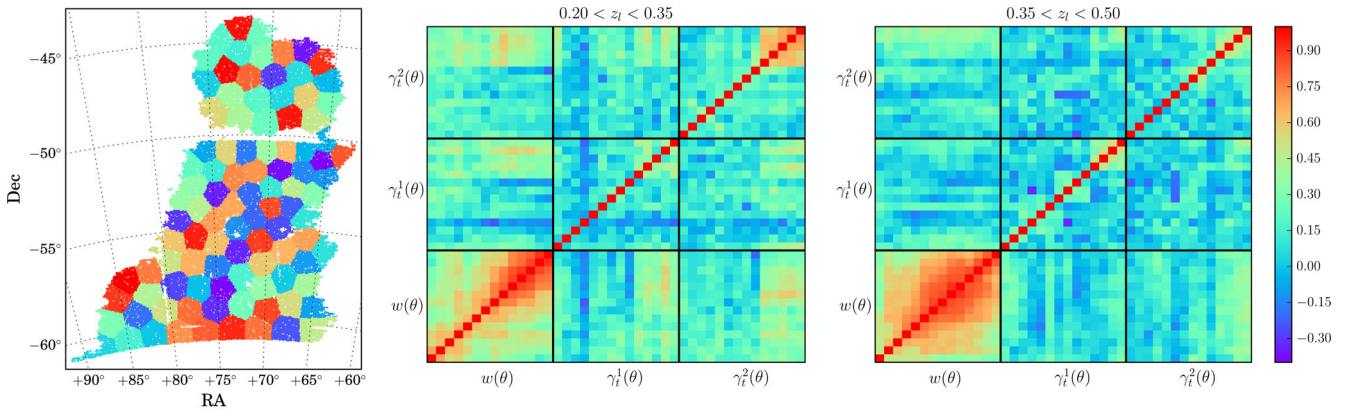

Figure 3. Left-hand panel: DES-SV SPT-E footprint and an example of the KMEANS jackknife regions used to compute the covariance matrices used in this work. Centre panel: for the first lens bin, the joint jackknife correlation matrix for $w(\theta)$ and $\gamma_t(\theta)$ for the two source bins. For each submatrix of the joint correlation matrix, the angular scale ranges from 4 to 100 arcmin in logarithmic bins. Right-hand panel: same as the centre panel, for the second lens bin.

lens–source pairs. For our measurements, we compute the average in angular separation bins, θ, so that

$$\langle \gamma_t(\theta) \rangle = \frac{\sum_j \omega_j \gamma_{t,j}}{\sum_j \omega_j}, \tag{13}$$

where the tangential shear for each lens–source pair, j, is weighted by a factor ω_j as follows:

$$\omega_j = \frac{1}{\sigma^2_{\rm shape} + \sigma^2_{{\rm m},j}}, \tag{14}$$

where $\sigma_{\rm shape}$ is the shape noise intrinsic to each background galaxy, and $\sigma_{{\rm m},j}$ is the error derived from the shape measurement. We use $\sigma_{\rm shape} = 0.233$ for the IM3SHAPE shear catalogue and $\sigma_{\rm shape} = 0.243$ for the NGMIX shear catalogue. The weights ω_j corresponding to the shear catalogues used in this work are computed and described in Jarvis et al. (2016). In order to correct for possible geometric and additive shear systematic effects, we compute the tangential shear around random lenses and subtract this from the galaxy lensing signal [as in Clampitt et al. (2016)]. The result is shown in the lower panels of Fig. 2, over the same range of scales as for $w(\theta)$. For each lens bin, we show the tangential shear using the two source bins.

3.2 Covariances

Our measurements of $w(\theta)$ and $\gamma_t(\theta)$ are correlated across angular and source redshift bins. The joint covariance for all the measurements corresponding to each lens redshift bin is estimated from jackknife (JK) resampling, using the following expression (Norberg et al. 2009):

$$C(x_i, x_j) = \frac{(N_{\rm JK} - 1)}{N_{\rm JK}} \sum_{k=1}^{N_{\rm JK}} (x_i^k - \bar{x}_i)(x_j^k - \bar{x}_j), \tag{15}$$

where the complete sample is split into a total of $N_{\rm JK}$ groups, x_i^k is a measure of the statistic of interest in the ith bin using all JK regions excepting the kth sample, and $\bar{x}_i$ is the mean of $N_{\rm JK}$ resamplings. Jackknife regions are obtained using the KMEANS algorithm[5] run on a homogeneous random points catalogue and, then, all catalogues (lenses, sources and random points) are split in $N = 100$ JK samples. KMEANS is a clustering algorithm that subdivides n observations into N clusters [see appendix B in Suchyta et al. (2016) for details]. By applying it to a uniform random catalogue with the same sky coverage as DES-SV, we define regions that are well suited for JK subsampling. The left-hand panel in Fig. 3 shows our JK patches created by the KMEANS algorithm. The resulting covariance matrices for both lens bins are also shown in Fig. 3 (centre and right-hand panels). The covariance is strongest between points within the $w(\theta)$ data vector. Note that: (i) we do not jointly fit both lens bins in the fiducial case so no covariances between lens bins are shown, and (ii) when performing cosmology fits with the lower (higher) lens bin we only use 21 (24) data points (see Section 5.1).

The JK covariance matrices shown in Fig. 3 contain a non-negligible level of noise. Hartlap, Simon & Schneider (2007) showed that the inverse of an unbiased but noisy estimator of the covariance matrix is actually *not* an unbiased estimator of the inverse covariance matrix. Therefore, when using a JK covariance matrix, a correction factor of $(N_{\rm JK} - N_{\rm bins} - 2)/(N_{\rm JK} - 1)$ should be applied to the inverse covariance, where $N_{\rm JK}$ is the number of jackknife regions and $N_{\rm bins}$ is the number of measurements (Hartlap et al. 2007). We include this correction factor in all our cosmology results.

The performance of JK covariances in DES-SV has been studied separately for galaxy clustering and galaxy–galaxy lensing in Crocce et al. (2016), Giannantonio et al. (2016), and Clampitt et al. (2016), respectively. There we generally find good agreement between true covariances from simulations or theory and the JK estimates, especially at small scales. At large scales the comparison points to an overestimation of the covariance by the JK method in the lensing case.

We have tested our method of estimating JK covariances and in particular the Hartlap correction factor, by generating a number of lognormal realizations of the convergence and matter density fields, as described in Friedrich et al. (2016). These mocks were constructed to match the lens and source galaxy densities and survey area of the DES-SV region. We used 600 mocks as an estimate of the 'true' covariance and as well as a subset of 100 mocks to represent a noisy covariance derived from independent samples. A comparable JK covariance was generated from a lognormal mock at random and dividing it into 100 patches using the same algorithm as the DES-SV data. We found that error in applying the Hartlap correction to JK samples instead of independent mocks is only a few per cent compared to the total difference between using JK samples and independent samples.

[5] https://github.com/esheldon/kmeans_radec

Table 1. Parameters and their corresponding priors used in this work. Not all parameters are allowed to vary in every analysis. Nuisance parameters are contained in the lower half of the table. When choosing a prior range on cosmological parameters, we allowed a sufficiently wide range to contain all of the 2σ posterior on Ω_m, σ_8, w, and h, with *Planck* priors on Ω_b and n_s, for which we have less sensitivity. For the systematic parameters, our choice of prior range is informed from previous DES analyses that studied the effect of shear calibration (Jarvis et al. 2016), photo-z distributions (Bonnett et al. 2016), and intrinsic alignment contamination (Clampitt et al. 2016; The Dark Energy Survey Collaboration et al. 2016a) on the SV catalogues. The prior on the bias parameters were taken from studies of the redMaGiC mock catalogue (see Section 5.1 for details). In addition to the prior range on the nuisance parameters for the shear calibration and photo-z bias, there is a Gaussian prior centred around zero of width 0.5, as explained in the text.

Parameter	Prior Range	
Ω_m	0.1–0.8	Normalized matter density
Ω_b	0.04–0.05	Normalized baryon density
σ_8	0.4–1.2	Amplitude of clustering (8 h^{-1} Mpc top hat)
A_s	$1.0 - 4.0 \times 10^{-9}$	Amplitude of clustering of primordial power spectrum at pivot scale of 0.05 Mpc^{-1}
n_s	0.9–1.0	Power spectrum tilt
w	−5 to −0.33	Equation-of-state parameter
h	0.5–1.0	Hubble parameter ($H_0 = 100h$)
τ	0.04–0.12	Optical depth
b_1	1.0–2.2	Linear galaxy bias
b_2	−1.5 to 1.5	Next order bias parameter
β_i	−0.3 – 0.3	Shift in photo-z distribution (per source bin)
m_i	−0.2 to 0.2	Shear multiplicative bias (per source bin)
m_{IA}	−0.3 to 0.35	Intrinsic alignment amplitude (low-z source bin only)
α	−5 to −1	Additive constant $w(\theta) \rightarrow w(\theta) + 10^{\alpha}$

In this work, we also estimate the cross-covariance between galaxy clustering and galaxy–galaxy lensing, for which we find a small positive correlation among all clustering scales and large galaxy–galaxy lensing scales – the regime where the lensing errors are no longer dominated by shape noise. This is consistent with related previous work like Mandelbaum et al. (2013), where they were able to neglect this contribution due to their different noise properties. However, Marian, Smith & Angulo (2015) found a significant non-zero cross-correlation between angular clustering and galaxy–galaxy lensing, that could contribute to biased and over optimistic constraints if ignored. As a check on the amount of covariance between probes, Fig. 6 also shows the result of ignoring the cross-covariance on the constraints on Ω_m and σ_8. The derived cosmology shows little deviation from our fiducial results and we find that our constraints are only minimally stronger on σ_8 (by about 3 per cent) and weaker on Ω_m (also ∼3 per cent) with a 2 per cent improvement on $S_8 = \sigma_8(\Omega_m/0.3)^{0.16}$. This shows that the impact of the correlation between probes is subdominant to the covariance within the same probe.

4 FIDUCIAL COSMOLOGICAL CONSTRAINTS

In this section, we present our fiducial DES-SV cosmological constraints from a joint analysis of clustering and galaxy–galaxy lensing. The data vector consists of $w(\theta)$ and the two $\gamma_t(\theta)$ measurements for the $0.35 < z < 0.5$ redMaGiC bin (see Fig. 2), over angular scales of 17–100 arcmin. We chose this lens bin as our fiducial, as we estimate greater contamination from systematic errors, on both the clustering and lensing side, for the $0.2 < z < 0.35$ redMaGiC bin [see Section 5.6 and Clampitt et al. (2016)]. To compute the model we use CAMB (Lewis, Challinor & Lasenby 2000; Howlett et al. 2012) and HALOFIT (Smith et al. 2003; Takahashi et al. 2012) for the linear and nonlinear matter power spectra, respectively. Because the accuracy of HALOFIT can be confirmed only to ∼5 per cent for certain ΛCDM models, we have checked that using the COSMIC EMULATOR, a more precise modelling scheme for the non-linear dark matter power spectrum (1 per cent to $k = 1$ Mpc^{-1}, Lawrence et al. 2010) would only affect our results at the level of ∼5 per cent down to 10 arcmin. We use the COSMOSIS package[6] (Zuntz et al. 2015) as our analysis pipeline and explore the joint posterior distribution of our cosmological (and nuisance) parameters using the MULTINEST Markov Chain Monte Carlo algorithm of Feroz, Hobson & Bridges (2009), with a tolerance parameter of 0.5, which controls the convergence of the chains, and an efficiency parameter of 0.8. Our cosmological parameters and priors are summarized in Table 1 and described in greater detail next in this section.

In the fiducial case, we have included two nuisance parameters per source bin (one for errors in the photo-z distribution and one for biases in the shear calibration) and one nuisance parameter per lens bin (the linear bias, b_1; the nonlinear bias, b_2, accounting for scale dependence and stochasticity, is studied in Section 5.1), plus an additional term, α, to account for potential systematic errors induced by observational effects that might induce an overall shift in the normalization of the amplitude of $w(\theta)$ (see Section 5.6). The full set of nuisance parameters and their priors are listed in the lower half of Table 1 and summarized below.

(i) *Photometric redshift calibration*. For each source bin i, we marginalize over a photo-z bias parameter, β_i, defined such as $n_i(z) \rightarrow n_i(z + \beta_i)$. In Bonnett et al. (2016), it was found that a single additive parameter for the photo-z distribution with a Gaussian prior centred on zero with a dispersion of 0.05, was sufficient to account for any statistical bias on Σ_{crit} and hence σ_8 within the degree of statistical error expected for the SV catalogues.

(ii) *Shear calibration.* For each source bin i, we marginalize over an extra nuisance parameter m_i, to account for the shear calibration uncertainties, such that $\gamma_{t;i}(\theta) \rightarrow (1 + m_i)\,\gamma_{t;i}(\theta)$, with a Gaussian prior with mean 0 and width 0.05, as advocated in Jarvis et al. (2016).

(iii) *Additive* w(θ) *constant*. We marginalize over an additive constant parameter, α, in the galaxy angular correlation function: $w(\theta) \rightarrow w(\theta) + 10^{\alpha}$. This parameter accounts for possible systematics arising from variations in observing conditions across the

[6] https://bitbucket.org/joezuntz/cosmosis

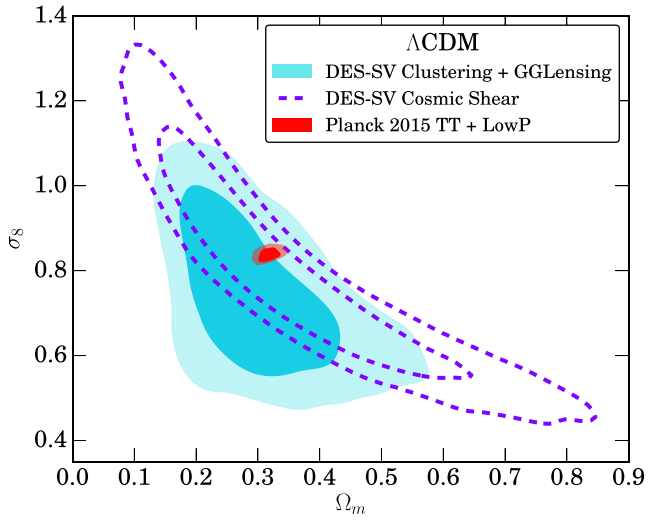

Figure 4. Constraints on Ω_m and σ_8 using DES-SV Cosmic Shear (dashed purple), DES-SV $w(\theta) \times \gamma_t(\theta)$ (this work, filled blue) and Planck 2015 using a combination of temperature and polarization data (TT+lowP, filled red). In each case, a flat ΛCDM model is used.

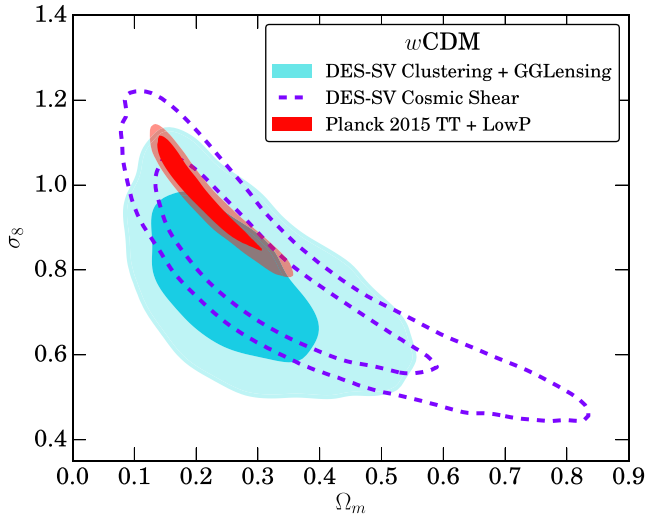

Figure 5. Constraints on Ω_m and σ_8 assuming a wCDM model using DES-SV Cosmic Shear (dashed purple), DES-SV $w(\theta) \times \gamma_t(\theta)$ (this work, blue) and Planck 2015 using temperature and polarization data (TT+lowP, red).

field, stellar contamination and masking (Ross et al. 2011), which we also test for in the next section.

The resulting constraints in the Ω_m and σ_8 plane are shown in Fig. 4. The 2D contours are centred around $\Omega_m \sim 0.3$ and $\sigma_8 \sim 0.75$, and marginalizing out the other parameter we find the following 1D constraints: $\Omega_m = 0.31 \pm 0.10$ and $\sigma_8 = 0.74 \pm 0.13$. Comparing to measurements from *Planck* (Planck Collaboration XIII 2016) and DES Cosmic Shear (The Dark Energy Survey Collaboration et al. 2016a) alone, we are consistent at the $\sim 1\sigma$ or better level. We combine results from the two experiments in Section 6. In addition, we see the same direction of degeneracy between these two parameters as with cosmic shear, although the degeneracy is not quite as strong with $w(\theta)$ and $\gamma_t(\theta)$.

We also include w, the dark energy equation-of-state parameter, as an additional free parameter in Fig. 5. We found that the DES-SV data alone was unable to provide strong constraints on w and obtained $w = -1.93 \pm 1.16$. However, compared to *Planck* (red contours), the DES-SV constraints on Ω_m and σ_8 are degraded far less when w is introduced as a free parameter. Also, we note that the preference for $w < -1$ values is determined by our choice of prior on w; we require $-5 < w < -0.33$, so the prior volume covered by $w < -1$ is greater than $w > -1$ and in the absence of a strong constraint on w, values of $w < -1$ are favoured.

Table 2 contains a more detailed summary of our findings for this fiducial setup, assuming either a ΛCDM or wCDM cosmology. In addition to DES $w(\theta)$ and $\gamma_t(\theta)$, we show results combined with *Planck*. Table 2 also shows results for our lower redshift lens bin, $0.2 < z < 0.35$. For these results we vary only the cosmological parameters $\{\Omega_m, \Omega_b, h, n_s, \sigma_8\}$ and w where noted (in addition to the nuisance parameters described in the present and following sections). When combined with constraints from *Planck*, we also allow the optical depth, τ, to vary as well, since the Cosmic Microwave Background (CMB) has additional sensitivity to physics that is only weakly captured by large-scale clustering at late times and we fit for the amplitude of the primordial power spectrum, A_s, rather than σ_8. Table 3 shows the constraints on the nuisance parameters related to photo-z and shear calibration described above.

In the following section, we will study the robustness of these results under changes in the configuration of the data vector and the systematics modelling.

5 ROBUSTNESS OF THE RESULTS

In this section, we describe the suite of tests performed to check that our conclusions are unbiased with respect to errors in the shear and photo-z calibrations, intrinsic alignments (IAs), survey geometry, choice of angular scales and theoretical modelling of the data vectors. The results in this section are displayed in Fig. 6, for the parameters we are most sensitive to in this work: $\{\Omega_m, \sigma_8, b_1\}$. The different rows correspond to the different tests described in this section or in the Appendix, where we check the results from a different lensing estimator. Despite the changes in the photo-z algorithms, the shear catalogues, the weighting of the lens–source pairs, nonlinear bias modelling and choice of scale, our estimates for these cosmological parameters in Fig. 6 usually remain within 1σ of the fiducial constraints.

A number of systematics that are unique to the measurement of the tangential shear such as the calibration of galaxy ellipticities, the effect of different shear calibration pipelines, null detection of the cross component, and effect of photo-z errors in the lens and source catalogues on the measurement have already been accounted for in Clampitt et al. (2016), so we do not present tests for these effects again. For more information on tests of the shear pipeline, we refer the reader to Jarvis et al. (2016) while Bonnett et al. (2016) contains extensive tests of the photo-z calibration algorithms. We also check for possible systematics introduced by the effects of survey geometry, depth and varying observing conditions in the survey following the techniques in Crocce et al. (2016).

Our analysis pipeline accounts for the effect of a number of systematics which are folded into our final constraints on cosmology. To first order, these nuisance parameters are responsible for altering the amplitude of $w(\theta)$ and $\gamma_t(\theta)$, and so are strongly degenerate with one another. As a result, we were unable to constrain these parameters beyond their prior distributions and the results in Table 3 show that the posterior distributions of the nuisance parameters no more informative than the priors. To determine which of these most affect our results, we have analysed each of these systematics individually by running chains in four scenarios: no systematics, shear

Table 2. Marginalized mean cosmological parameters (and 1σ errors) measured from the posterior distribution of a joint analysis of angular clustering and galaxy–galaxy lensing. Results for DES-SV data alone and in combination with *Planck* and external data (BAO, SN1a, H0) are shown for the two-lens redshift bins both separately and combined. (Note that the biases are quoted separately: $b_1 = 1.52 \pm 0.28$ for $0.2 < z < 0.35$ and $b_1 = 1.60 \pm 0.27$ for $0.35 < z < 0.5$). Not shown are the additional cosmological parameters that we have marginalized, $\{n_s, \Omega_b, h_0\}$ as well as our standard set of nuisance parameters. Also quoted are the mean values and 1σ errors given by *Planck* (TT+lowP) and external data alone.

Probes	z	σ_8	Ω_m	$S_8 \equiv \sigma_8(\Omega_m/0.3)^\alpha$	α	b_1	w_0
DES	$0.2 < z < 0.35$	0.73 ± 0.12	0.46 ± 0.12	0.77 ± 0.11	0.15	1.60 ± 0.31	-1
DES	$0.2 < z < 0.35$	0.74 ± 0.13	0.41 ± 0.14	0.77 ± 0.10	0.17	1.73 ± 0.29	-2.5 ± 1.26
DES	$0.35 < z < 0.5$	0.74 ± 0.13	0.31 ± 0.09	0.74 ± 0.12	0.16	1.64 ± 0.30	-1
DES	$0.35 < z < 0.5$	0.77 ± 0.12	0.28 ± 0.10	0.75 ± 0.11	0.13	1.71 ± 0.28	-2.03 ± 1.19
DES	$0.2 < z < 0.5$	0.76 ± 0.10	0.36 ± 0.09	0.78 ± 0.09	0.21	1.52 ± 0.28 1.60 ± 0.27	-1
Planck		0.83 ± 0.01	0.32 ± 0.01	0.82 ± 0.02	-0.49		-1
Planck		$0.98^{+0.11}_{-0.06}$	$0.21^{+0.02}_{-0.07}$	1.21 ± 0.27	-0.6		$-1.54^{+0.20}_{-0.40}$
BAO + SN + H0			0.33 ± 0.02				-1.07 ± 0.06
BAO + SN + H0 + DES	$0.35 < z < 0.5$	0.71 ± 0.1	0.32 ± 0.02	0.71 ± 0.1	0.01		-1.05 ± 0.07
DES + *Planck*	$0.2 < z < 0.35$	0.84 ± 0.01	0.35 ± 0.01	0.76 ± 0.02	-0.71	1.30 ± 0.13	-1
DES + *Planck*	$0.2 < z < 0.35$	0.89 ± 0.03	0.32 ± 0.02	0.84 ± 0.06	-0.76	1.25 ± 0.13	-1.16 ± 0.09
DES + *Planck*	$0.35 < z < 0.5$	0.84 ± 0.01	0.35 ± 0.01	0.76 ± 0.02	-0.71	1.41 ± 0.17	-1
DES + *Planck*	$0.35 < z < 0.5$	0.88 ± 0.03	0.32 ± 0.02	0.84 ± 0.06	-0.75	1.36 ± 0.14	-1.14 ± 0.09
DES + *Planck* + BAO + SN + H0	$0.35 < z < 0.5$	0.86 ± 0.02	0.31 ± 0.01	0.84 ± 0.03	-0.81	1.74 ± 0.28	-1.09 ± 0.05

Table 3. Marginalized mean systematic uncertainty parameters with 1σ errors measured from the posterior distribution of the joint analysis of angular clustering and galaxy–galaxy lensing in DES-SV data. We assume a Gaussian prior (centred on zero) for each systematic parameter, while the width of the prior is set from Jarvis et al. (2016) for the shear calibration and Bonnett et al. (2016) for the photo−zs. Each nuisance parameter is additionally truncated by the amounts in Table 1.

Probes	z	$100\beta_1$	$100\beta_2$	$100m_1$	$100m_2$	α
DES (ΛCDM)	$0.2 < z < 0.35$	-0.89 ± 4.58	0.25 ± 4.56	-0.09 ± 4.59	0.44 ± 4.42	-3.41 ± 0.84
DES (wCDM)	$0.2 < z < 0.35$	-1.00 ± 4.53	0.13 ± 4.51	-0.85 ± 4.47	0.14 ± 4.57	-3.42 ± 0.83
DES (ΛCDM)	$0.35 < z < 0.5$	-1.77 ± 4.46	0.14 ± 4.67	-0.05 ± 4.65	0.36 ± 4.64	-3.57 ± 0.81
DES (wCDM)	$0.35 < z < 0.5$	-1.78 ± 4.38	0.18 ± 4.48	-0.85 ± 4.48	0.05 ± 4.31	-3.49 ± 0.81
DES + *Planck* (ΛCDM)	$0.2 < z < 0.35$	-0.58 ± 4.83	0.29 ± 4.99	-0.63 ± 4.87	0.72 ± 4.84	-3.62 ± 0.82
DES + *Planck* (wCDM)	$0.2 < z < 0.35$	-0.87 ± 4.73	0.14 ± 4.87	-0.76 ± 4.88	0.41 ± 4.79	-3.62 ± 0.82
DES + *Planck* (ΛCDM)	$0.35 < z < 0.5$	-3.11 ± 4.48	-0.53 ± 4.95	-0.99 ± 4.92	-0.65 ± 4.77	-3.44 ± 0.87
DES + *Planck* (wCDM)	$0.35 < z < 0.5$	-1.04 ± 2.53	-0.16 ± 2.64	-1.09 ± 4.32	-0.68 ± 4.34	-3.43 ± 0.85

calibration only, photo-z errors only, full weak-lensing systematics but no constant offset in w(θ), and shear calibration with photo-z errors (our fiducial set up). We found that including an additive constant to $w(\theta)$ was responsible for the greatest decrease in precision on the 1D marginalized constraints on Ω_m, with the 1σ error on Ω_m increasing by as much as 17 per cent compared to the no systematics case. However, σ_8 was much less affected with a difference below 3 per cent. In comparison, accounting for photo-z errors with an additional two free parameters in the $N(z)$ distribution increased the error on both parameters by about 8 per cent. The change from including two shear calibration parameters was smaller still, with only a 3 per cent reduction in precision for Ω_m and 5 per cent for σ_8 relative to the no systematics case. We also found small changes to the best-fitting values, well within the 1σ confidence interval, as expected from Fig. 6.

5.1 Choice of scales

There are several reasons to limit the range of scales that we consider in our analysis. The large-scale cutoff is set by the size of the SV patch and how well the geometry of the region can be modelled; we found that our jackknife estimates of the covariance matrix overestimated the covariance matrix obtained from 50 independent N-body simulations above 70 arcmin (see Fig 5; Clampitt et al. 2016).

On small scales, we are limited by how well we can model the non-linear clustering of matter and redMaGiC galaxies. Galaxy formation preferentially occurs in high-density environments within dark matter haloes and is subject to a number of complex baryonic processes; these are not captured in our model predictions for the mass power spectrum and potentially introduce a non-trivial bias between the dark matter and the galaxies. This is particularly important for the tangential shear, which contains a mixture of small- and large-scale information; i.e. imposing a sharp cutoff in angular scale does not completely eliminate the effect of scales below that cutoff (Mandelbaum et al. 2013). On small enough scales, we expect to observe effects such as stochasticity, non-local bias and scale dependence. These could invalidate the linear bias model used in our analysis.

In this section, we present simulation-based tests to determine the smallest scales for which the linear bias model and perturbation theory model of McDonald (2006) are valid. We use a mock catalogue designed to reproduce the properties of the DES-SV survey. The catalogue is based on an N-body simulation (c-400; see also Mao, Williamson & Wechsler 2015; Lehmann et al. 2015) run with the L-GADGET code, a variant of GADGET (Springel 2005). The simulation

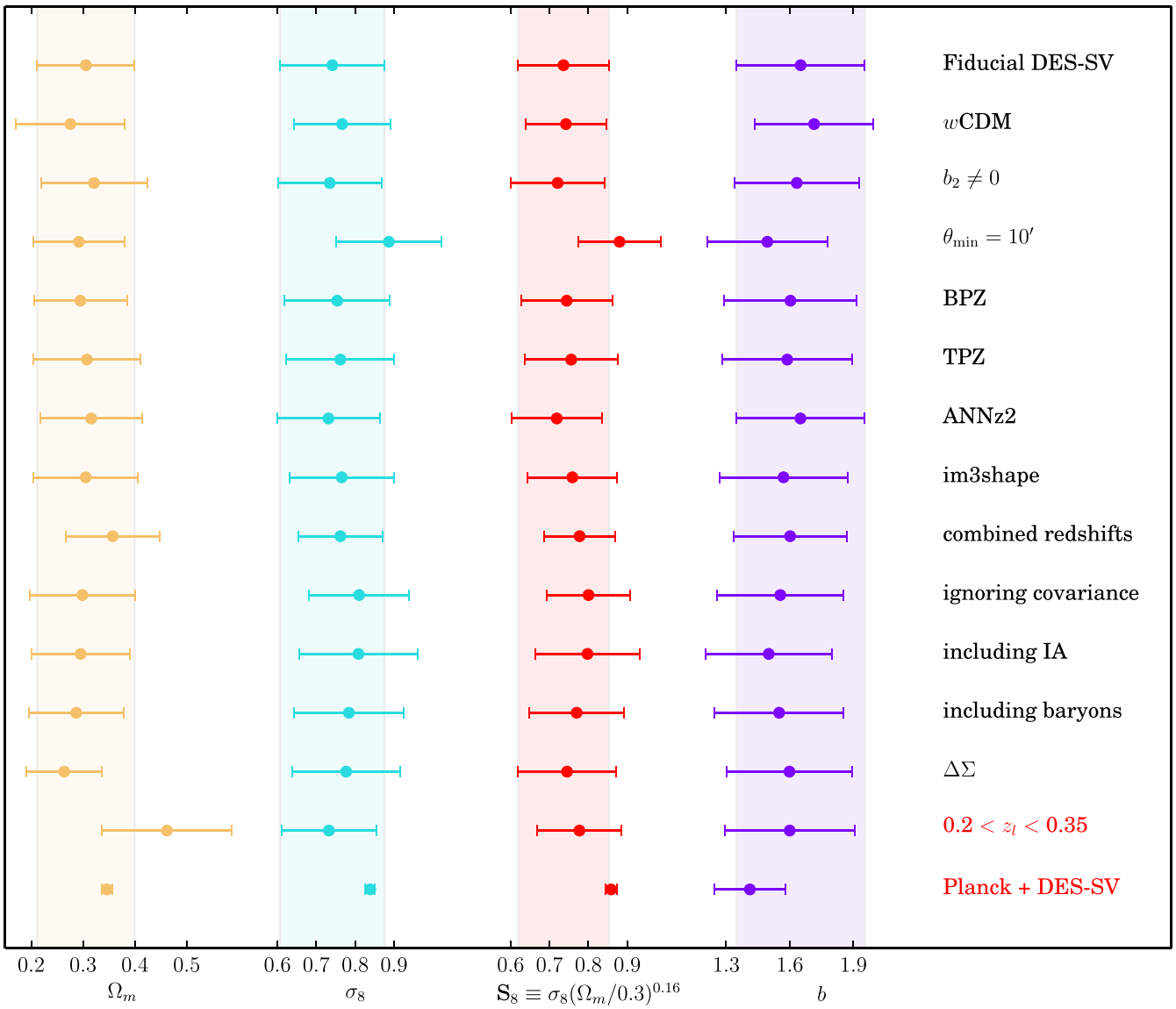

Figure 6. Marginalized 1D posterior constraints on $\{\Omega_{\rm m}, \sigma_8, S8, b_1\}$ for the lens bin $0.35 < z < 0.5$ for various configurations in our pipeline. For this figure, we have defined $S_8 \equiv \sigma_8(\Omega_{\rm m}/0.3)^{0.16}$, that is, we hold the index fixed to the degeneracy direction found for our fiducial analysis. Note that this value is substantially different to one favoured by *Planck* data alone, but we have chosen a constant value to enable comparisons between the systematic tests. Our fiducial results use shear catalogues from NGMIX, SKYNET photometric redshifts, and linear bias in a ΛCDM cosmology, as described in Section 4. The different rows in this plot are obtained by varying the fiducial assumptions individually to test their impact on the parameter constraints, and they are all detailed in Section 5 and the Appendix. Tests involving (nearly) independent data are highlighted in red near the end of the table.

has a box size of 400 Mpc h^{-1} with 2048^3 particles and a force resolution of 5.5 kpc h^{-1}. Halo catalogues were generated with the ROCKSTAR halo finder (Behroozi, Wechsler & Wu 2013a) and the CONSISTENT TREES merger tree builder (Behroozi et al. 2013b). A galaxy catalogue was produced using an abundance matching technique, as described in Reddick et al. (2013) and Lehmann et al. (2015), with haloes ranked according to the peak halo velocity and assigned a luminosity from the Blanton et al. (2003) luminosity function, using a scatter of 0.2 dex. Snapshots from the simulation were combined into a light-cone with the same footprint as the DES-SV region. Galaxy colours were assigned using the empirically derived relationship between luminosity, projected distance to the fifth nearest neighbour galaxy, and galaxy SED [this method for assigning colours has been used in previous generations of catalogues, see e.g. Cunha et al. (2012) and Chang et al. (2015)]. Photometric errors were added to match the depth distribution of the DES-SV galaxies. The redMaGiC algorithm was run on the light-cone, using the same technique as applied to the DES-SV data and this produced a mock redMaGiC catalogue. The redMaGiC colour model is retuned to the simulations before identifying these galaxies, but was found to have similar properties to that seen in the data. We find that the clustering properties of the redMaGiC galaxies in this catalogue are consistent with those measured in the DES-SV data.

From the mock catalogue, we have measured $w(\theta)$ in the same bins in redshift, $0.2 < z < 0.35$ and $0.35 < z < 0.5$, from 10 arcmin $< \theta <$ 100 arcmin. Our covariance matrix is calculated from a jackknife resampling of the catalogue as described in Section 3.2.

We test our bias modelling by making two cuts in angular scale at 10 arcmin and 17arcmin, corresponding to ($\sim$ 3 Mpc h^{-1}) and

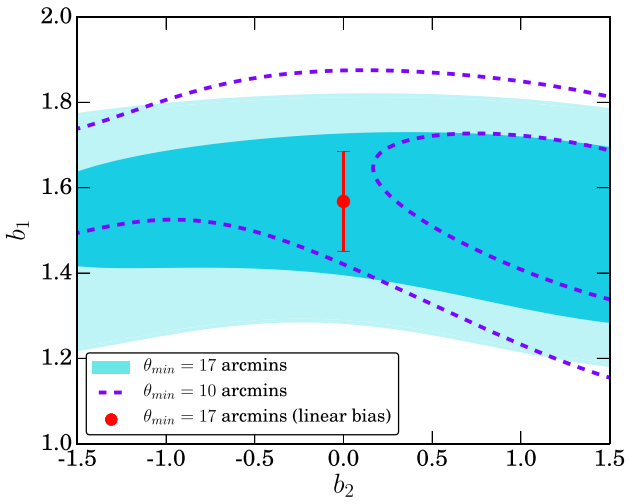

Figure 7. The posterior distribution on the bias parameters, b_1, b_2 from simulations of $w(\theta)$ for the redshift bin $0.35 < z < 0.5$. We fit the McDonald (2006) model to a minimum cut in scale at 10 arcmin (cyan) and 17 arcmin (purple) and a linear bias model to 17 arcmin (red point) to demonstrate the insensitivity of our fiducial results with a 17 arcmin cutoff to b_2.

(~ 5.5 Mpc h^{-1}), because we expect the bias to transition between its large-scale asymptotic limit to scale dependence somewhere in this regime for the galaxy type that we consider. We fit both a linear and a quasi-linear bias model with two free parameters, b_1 and b_2, as described in Section 2.1 to the simulated $w(\theta)$ while holding the cosmological parameters fixed to the value of the N-body simulation. Note that the effect of the shot noise parameter, N, on $w(\theta)$ is negligible on our scales of interest so we do not include it in our tests. Fig. 7 shows the recovered biases when all the cosmological parameters are fixed at the simulation values for the fiducial lens bin of $0.35 < z < 0.5$. The measured $w(\theta)$ is insensitive to the value of b_2 when a minimum angular scale of 17 arcmin is chosen (cyan filled contour) and we are simply recovering our prior distribution on b_2.

When we change the minimum scale to 10 arcmin (purple dashed contour), there is a 1σ preference for a non-zero value. Using a linear model of biasing (Fig. 7; red point) with the same fixed cosmology set up, we find that we recover the same value of b_1 as in the nonlinear case. We obtain similar results for the low-z lens bin, except that the minimum scale cutoff is now at 22 arcmin for $w(\theta)$ to be well modelled by a linear bias. Fig. 7 demonstrates that our choice of using a linear bias up to these angular scales for the redMaGiC sample should not affect our ability to constrain cosmology. Based on these results, we can conclude that applying a linear bias model with $\theta_{\rm min} = 17$ arcmin (22 arcmin) for the high-z (low-z) lens bin will not bias our results in the presence of scale dependent nonlinear biasing. Since our simulations do not address the lensing component of our analysis, we have performed to additional checks using the data. We have rerun our fiducial analysis with b_2 as an additional free parameter, while keeping $\theta_{\rm min} = 17$ arcmin. For these fits, we obtained $\Omega_{\rm m} = 0.32 \pm 0.10$, $\sigma_8 = 0.73 \pm 0.13$, $b_1 = 1.63 \pm 0.29$, and $b_2 = -0.14 \pm 0.76$, which is consistent with our fiducial results. We have also tested our small-scale cutoff by using $\theta_{\rm min} = 10$ arcmin with our fiducial set up. We found that this increased the value of σ_8 to 0.887 ± 0.134 from $\sigma_8 = 0.741 \pm 0.134$. Since the decrease in the error bars on our cosmological parameters of interest is not significant, we kept our existing value of $\theta_{\rm min}$ to 17 arcmin.

For the shear catalogues, Jarvis et al. (2016) identified 3 arcmin as the angular scale in the shear autocorrelation function at which the additive errors contribute to half of the total forecasted error on the measurement of σ_8 or about $\sim$3 per cent. Although it is expected that position–shear correlations are less sensitive to additive systematics in the shear, we only consider angular scales $\theta \geq 10$ arcmin even for the tests of the bias model above. This 3 arcmin cutoff is well outside of the minimum scales considered in our cosmological analysis which use at most $\theta > 17$ arcmin.

5.2 Photo-z systematics

Since DES-SV is an imaging survey, the quality of our constraints rely heavily on being able to robustly calibrate the photometric redshifts of the lens and source galaxy samples. However, because $w(\theta)$ does not use radial information, apart from the selection function, it is relatively insulated from photometric errors compared to the full 3D correlation function. Furthermore, because the photometric error in the lens redMaGiC sample is so small (Rozo et al. 2016), the potential systematic errors in the cosmology analysis are dominated by the photometric redshifts of the source galaxy sample.

We deal with photometric redshift systematics in two different ways. First, we follow the recommendations of Bonnett et al. (2016) and define an additional photo-z bias parameter for each source bin, i, as:

$$n_i^{\rm pred}(z) = n_i^{\rm obs}(z + \beta_i)\,, \tag{16}$$

where β_i is a free parameter with a Gaussian prior of width 0.05 to be constrained during the fitting process. The width of the prior is set to be consistent with Bonnett et al. (2016), where it was found that the difference between photometric and spectroscopic estimates of the redshift of the training samples that most closely resemble our shear catalogues have a relative mean bias with a Gaussian dispersion of 0.05. This method was also used in the DES-SV Cosmic Shear Cosmology paper (The Dark Energy Survey Collaboration et al. 2016a). We found that introducing an additional photo-z bias parameter for each source bin increases our uncertainty by, at most, 8 per cent compared to the constraints we would have if we did not fit for any systematic parameters.

In addition, we check that our constraints are robust to our choice of photo-z algorithm. Our fiducial shear catalogues use photometric redshifts derived from the SKYNET algorithm (Graff et al. 2014; Bonnett et al. 2016), and we have repeated our analysis by using the redshift distribution given by three other photo-z codes studied in Bonnett et al. (2016), namely BPZ, TPZ and ANNZ2. For this test, we assume a ΛCDM cosmology and allow the cosmological parameters $\{\Omega_{\rm m}, \Omega_{\rm b}, h, \sigma_8, n_{\rm s}, b_1\}$ to vary. In addition, we also fit for the usual systematic parameters, β_i for the photo-z bias and m_i for the multiplicative bias in the shear calibration and the same prior distributions. The resulting constraints in Figs. 6 and 8 show that our results are insensitive to the choice of the photo-z algorithm.

Interested readers should refer to Bonnett et al. (2016) for a full discussion of the photo-z methods considered and the systematics modelling that we have only summarized here.

5.3 Shear calibration systematics

Here we present our approach to modelling a possible residual error in the shear calibration. For the interested reader, the full details of the production and testing of the shear catalogues used in this analysis are given in Jarvis et al. (2016).

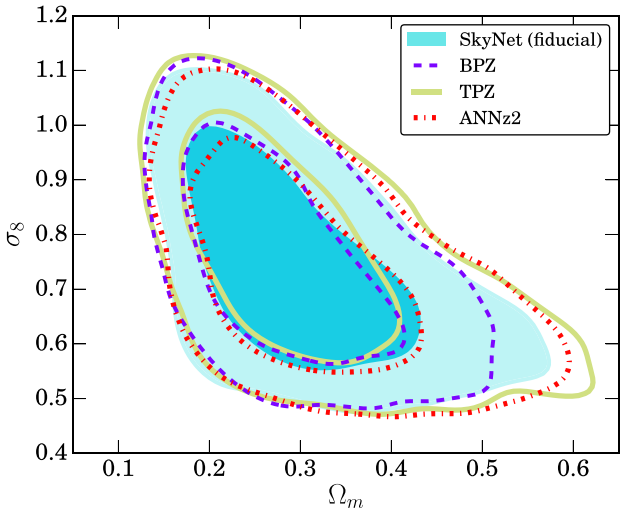

Figure 8. Constraints on Ω_m and σ_8 using four different photo-z codes to calculate the redshift distribution of sources. The contours for the $0.35 < z < 0.5$ redshift bin are shown here; we have also checked the robustness of our results for lenses in the redshift bin $0.2 < z < 0.35$.

Similar to the photometric redshift case, we deal with potential shear calibration systematics on two fronts. First, we include an extra nuisance parameter for the shear calibration, m_i, as:

$$\gamma_{t;i}^{\rm pred}(\theta) = (1 + m_i)\,\gamma_{t;i}^{\rm obs}(\theta) \tag{17}$$

with a Gaussian prior, $p(m_i)$, with mean 0 and width 0.05, for each source bin i in our analysis as recommended in Jarvis et al. (2016). Contamination from additive errors in the shear estimation are expected to be minimal for galaxy–galaxy lensing, because of the azimuthal symmetry of the lens system. Including an additional parameter for the shear calibration degrades our constraints by, at most, 5 per cent, compared to all systematic parameters being ignored or set to fixed values.

Secondly, galaxy images in the DES-SV region were analysed with two pipelines, NGMIX and IM3SHAPE. Jarvis et al. (2016) showed that they both produced consistent results that satisfied the SV requirements for weak lensing, i.e. that less than half of the forecasted error on σ_8 (about 3 per cent) originates from systematics in the measurement of the shear. Although we have chosen to use the NGMIX catalogue for our analysis, we have also rerun the analysis pipeline on the IM3SHAPE catalogue to check that our results are not sensitive to the shear catalogue used (see Fig. B1 for a comparison of lensing measurements using the two shear pipelines). We found that the cosmological parameters varied imperceptibly when the IM3SHAPE catalogue was used instead of NGMIX. This is demonstrated in Fig. 6.

5.4 Intrinsic alignments

Correlations between the intrinsic shapes and orientations of lensing sources, known as 'intrinsic alignments', are one of the most significant astrophysical sources of uncertainty in weak-lensing measurements [see Troxel & Ishak (2015) and Joachimi et al. (2015) for recent reviews]. Although typically considered in the context of shear–shear correlations, IA can also contaminate galaxy–galaxy lensing measurements due to uncertainties in photo-z estimates which lead to overlap in the true lens and source distributions (see Fig. 1). The intrinsic shapes of sources can be correlated with the positions of lenses at the same redshift (Blazek et al. 2012).

In general, the contamination from IA reflects the (potentially non-linear) relationship between large-scale structure and galaxy shapes, as well as the clustering of lenses and physically associated sources. However, observational evidence (e.g. Blazek, McQuinn & Seljak 2011; Joachimi et al. 2011; Singh & Mandelbaum 2015) indicates that the dominant IA contribution is likely from elliptical (pressure-supported) galaxies, for which the IA component is linearly related to the large-scale tidal field. This 'tidal alignment' paradigm (Catelan, Kamionkowski & Blandford 2001; Hirata & Seljak 2004; Blazek, Vlah & Seljak 2015) was recently used to mitigate IA in the DES-SV Cosmic Shear Cosmology analysis (The Dark Energy Survey Collaboration et al. 2016a). In this work, we consider scales on which the clustering of lens–source pairs is negligible [see Clampitt et al. (2016) for further discussion]. In this regime, tidal alignment predicts that the fractional IA contamination to the lensing signal is nearly scale-invariant. Both the IA and lensing are sourced by the same matter power spectrum, even in the presence of non-linear evolution, and we find that the different line-of-sight weighting for IA and lensing [e.g. equation (3)] leads to negligible relative scale-dependence in angular correlations.

We thus account for the potential impact of IA in our analysis by including an additional term that modifies the amplitude of the tangential shear, such that $\gamma_t(\theta) \rightarrow (1 + m_{\rm shear\,cal} + m_{\rm IA})\gamma_t(\theta)$. We place a Gaussian prior on $m_{\rm IA}$ of 8 per cent ± 4 per cent for the lower redshift source bin, corresponding to the IA amplitude constraint of approximately $A_{\rm IA} = 2 \pm 1$ from the cosmic shear analysis of the same sources on the DES-SV patch (The Dark Energy Survey Collaboration et al. 2016a). The same calculation indicates that the higher redshift source bin is sufficiently separated from the redshift of the lenses that the potential IA contamination is negligible. Potential IA contamination in the galaxy–galaxy lensing measurement is discussed further in Clampitt et al. (2016).

We do not observe a significant detection of IA contamination beyond the prior imposed; we find that $m_{\rm shear\,cal,\,1} + m_{\rm IA,\,1} \sim 8.0 \pm 3.7$ per cent for the low-redshift sources with $m_{\rm shear\,cal,\,2} \sim -5.3 \times 10^{-4} \pm 4.5$ per cent for the higher source bin. Including IA only affects the cosmology results by, at most, inducing a $\sim$3 per cent shift towards a lower value of Ω_m compared to the fiducial case without IA, as shown in Fig 6. For σ_8, the change was much smaller, with a fractional shift of less than a percent. Because the inclusion of IA contamination has a negligible effect on our results, compared to the statistical errors, we do not include IA modelling for our fiducial analysis.

5.5 Impact of baryons

One of the most challenging sources of systematic error affecting weak-lensing results is the impact of baryonic effects on small-scale clustering. Much of the behaviour of baryonic content on small scales is unknown; the non-linear clustering can only be modelled by computationally expensive N-body simulations but the results vary greatly with the simulation parameters such as the amount of supernova and active galactic nuclei (AGN) feedback allowed. To minimize the impact of baryonic effects on our results, we choose to truncate our measurements conservatively to large scales. However, we have implemented a scheme for evaluating the effect of baryons on our results similar to that used for the DES cosmic shear analysis (The Dark Energy Survey Collaboration et al. 2016a). We take the power spectrum measured from the OWLS simulation (van Daalen et al. 2011) with AGN feedback, since this model induces the most extreme changes to small-scale clustering while also matching results of X-ray and optical observations (McCarthy et al. 2011),

and replaced the dark matter power spectrum evaluated by HALOFIT thusly:

$$P(k, z) \rightarrow \frac{P_{\rm AGN}}{P_{\rm DM}} P(k, z) \tag{18}$$

where $P_{\rm AGN}$ and $P_{\rm DM}$ are the power spectra measured from AGN and dark matter only models from the OWLS simulations, respectively. We found that including baryonic effects in this way, affects our results by a negligible amount as shown in Fig. 6 and the constraints shift to $\sigma_8 = 0.784 \pm 0.14$ and $\Omega_{\rm m} = 0.287 \pm 0.09$ from $\sigma_8 = 0.741 \pm 0.13$ and $\Omega_{\rm m} = 0.306 \pm 0.09$. For our fiducial results, we have chosen to ignore the impact of baryons.

5.6 Impact of observing conditions

Photometric galaxy surveys such as DES are affected by time-dependent fluctuations in observing conditions that may impact the galaxy catalogues. There are a number of effects that can modulate the detection efficiency of galaxies and cause density variations across the survey footprint. In this section, we follow the approach of Crocce et al. (2016) and consider single-epoch properties that affect the sensitivity of the survey and hence may affect the galaxy clustering and galaxy–galaxy lensing observables. We use projected HEALPIX[7] (Górski et al. 2005) sky maps (with resolution `nside`=4096) in *grizY* bands for the following quantities:

(i) `depth`: mean survey depth, computed as the mean magnitude for which galaxies are detected at $S/N = 10$.
(ii) `FWHM`: mean seeing, in pixel units, computed as the full width at half-maximum of the flux profile.
(iii) `airmass`: mean airmass, computed as the optical path length for light from a celestial object through Earth's atmosphere (in the secant approximation), relative to that at the zenith for the altitude of CTIO.
(iv) `skysigma`: mean sky background noise, computed as the flux variance per amplifier in chip of the CCD.
(v) `USNO`: mean stellar density, as measured by the USNO-B1 stellar catalogue (Monet et al. 2003) with *B* magnitude brighter than 20 to ensure constant depth across the field.

See Leistedt et al. (2016) for a full description of these maps.

We study the density of redMaGiC galaxies in the two-lens bins as a function of each of these quantities that can potentially result in systematic effects. To ensure the data are free of such systematics, we require the galaxy density to be uncorrelated with the observed `depth`, `FWHM`, `airmass`, `skysigma` and `USNO`, otherwise we apply a correction to remove the dependence. Among the five quantities for each band and each lens bin considered here, we only find a significant correlation in the low-z bin with `airmass` in the g and r DES bands. This trend is demonstrated in Fig. 9, which shows the redMaGiC galaxy density as a function of `airmass` in g, r and i bands for the two-lens bins. In order to correct for this correlation, we weight galaxies according to the inverse of a linear fit to the observed trend of `airmass` in the g band. This procedure is similar to that applied in Ross et al. (2012, 2014) to correct for systematic relationships with stellar density and `airmass`. The corrected results are shown in Fig. 9, where we see that the g band weighting also corrects the trend in the r band, as expected given the correlation present among the `airmass` maps in the g and r bands.

[7] http://healpix.sf.net

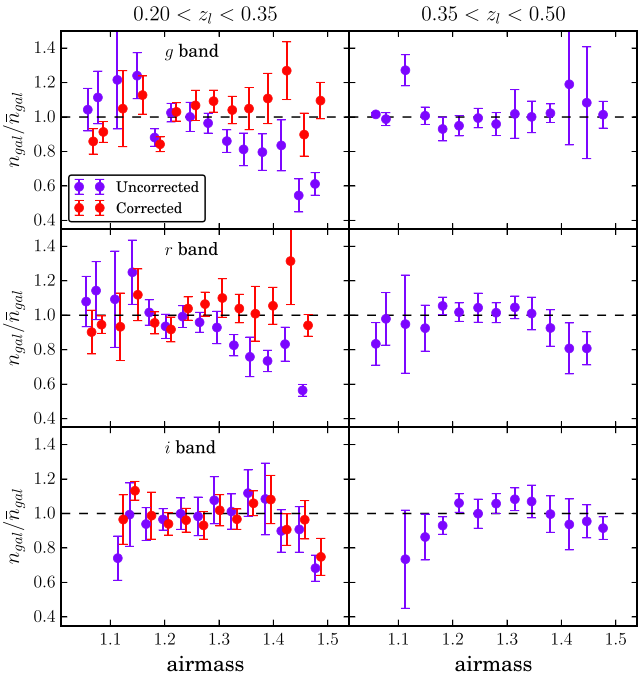

Figure 9. redMaGiC galaxy density as a function of `airmass` in g, r and i bands for the two-lens redshift bins considered in this work. A significant correlation is present for the g and r bands in the low-z bin, which we correct by weighting galaxies inversely by the `airmass` values at the sky position. Note that we do not apply a correction to the high-z bin since it does not show a significant correlation with any systematics parameter.

In addition to the weighting correction described above, we have also applied the procedure used in Crocce et al. (2016), in which galaxy and systematics maps are cross-correlated and used to correct the galaxy correlation functions. At the galaxy clustering level, the two approaches yield consistent results. Furthermore, in both cases the correction is compatible with an additive constant in the angular galaxy clustering signal. None the less, we introduce an additive constant as a systematics parameter in the corrected measurement of $w(\theta)$ as outlined in Section 4 to deal with any residual systematic effects. This is marginalized over the cosmological analysis according to the prior defined in Table 1. On the other hand, the impact of the `airmass` correction in the galaxy–galaxy lensing observables is not significant given the statistical power of these observations in DES-SV.

As opposed to Crocce et al. (2016) we do not find the `depth` and `FWHM` maps to be relevant for our lens sample, mainly because redMaGiC galaxies are much brighter than the DES main galaxy sample (Benchmark) considered in that work. On the other hand, correlations between `airmass` maps and galaxy positions were not found to be a significant systematic in Crocce et al. (2016), while for redMaGiC galaxies in the low-z lens bin, this was the only observing condition with a substantial impact on clustering. While Crocce et al. (2016) includes all types of galaxies, the redMaGiC selection process preferentially chooses red galaxies as described in Section 3. It is plausible that these galaxies are more affected by `airmass`, via their sensitivity to atmospheric extinction. At high `airmass`, the filter bandpasses shift to the red and the REDMAPPER colour selection, in which redMaGiC relies, do not compensate for this. The effect is more important for the bluer DES bands g and r (Li et al. 2016), and the key spectral features of red galaxies, like the 4000 Å break, fall in a bluer window of the filter set at lower

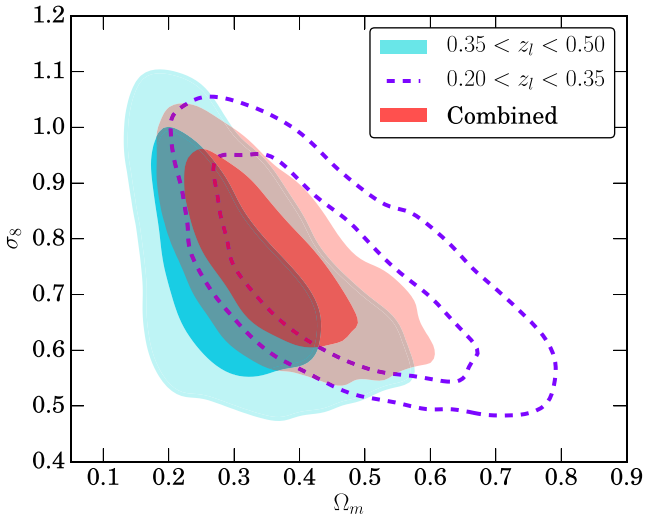

Figure 10. Constraints on Ω_m and σ_8 using DES-SV $w(\theta) \times \gamma_t(\theta)$. The fiducial high-$z$ lens bin is shown in filled blue, the low-z lens bin is shown as dashed purple lines and the combination of the two-lens bins is shown in filled red. In each case, a flat ΛCDM model is assumed.

redshifts, and hence the effect of atmospheric extinction is enhanced for our low-z lens bin.

In the following subsection, we present cosmology results with the low-z lens bin after correcting for the correlation with `airmass`.

5.7 Low-z lens bin results

In this section, we present the cosmology results obtained for the low-z redMaGiC lens bin ($0.20 < z < 0.35$), described in Section 3.1 and for which measurements are shown in Fig. 2. For this bin, a significant correlation of the galaxy density with `airmass` was found and corrected for in Section 5.6.

The photo-z and shear systematics treatment in the cosmology pipeline is equivalent to that of the fiducial lens bin and we use these results as another robustness check for the cosmological analysis performed in this work.

The cosmological constraints obtained from these measurements are shown in Fig. 6 and Table 2, and the constraints on Ω_m and σ_8 from the combination with the fiducial high-z lens bin are shown in Fig. 10. For most of the parameters, these lower redshift lenses are in agreement with our fiducial setup, but Ω_m shows a preference for higher values after correcting for the observing conditions described in Section 5.6. Still, the results for both lens bins are within 1σ of each other.

Having confirmed that the results from both the low- and high-redshift lens bins are consistent, we explore fitting them jointly in the same analysis pipeline to improve our constraints on cosmology. The covariance between lens bins may include a contribution from shape noise in the shear catalogue. We estimate this contribution by introducing a random direction to the measured ellipticities before calculating the tangential shear. This is performed ∼300 times to obtain a jackknife estimate of the shape noise across lens and source bins. We then add the shape noise as an off-diagonal component to the covariance matrix between lens bins with the diagonal components being the usual JK covariance matrices used for individual fits. We find that the marginalized constraints are $\Omega_m = 0.36 \pm 0.09$ and $\sigma_8 = 0.76 \pm 0.11$, which show very little improvement on our fiducial results. However, the constraint on $S_8 \equiv \sigma_8(\Omega_m/0.3)^\alpha$, where α is chosen to be perpendicular to the degeneracy direction in the Ω_m–σ_8 plane, shows a reduction in the error, from $S_8 = 0.735 \pm 0.117$ ($\alpha = 0.16$; high-z lenses only) to $S_8 = 0.782 \pm 0.088$ ($\alpha = 0.21$; all lenses). These values of Ω_m, σ_8 and S_8 are shown in Fig. 6. We do not however consider this arrangement as our 'fiducial' model, leaving joint constraints to future work with additional survey area.

6 DISCUSSION

We have presented our baseline cosmological results from DES data in Section 4, assuming a flat ΛCDM model in Fig. 4 and a flat wCDM model in Fig. 5. Our results for the marginalized mean parameter values are contained in Table 2 for each lens bin, with and without external data sets. We also show results for each of the nuisance parameters used in our fits in Table 3.

6.1 External data sets

We performed a joint analysis of our measurements with the Planck 2015 temperature and polarization auto and cross multipole power spectra, $C^{TT}(\ell)$, $C^{TE}(\ell)$, $C^{EE}(\ell)$, and $C^{BB}(\ell)$. Specifically, we use the full range of $C^{TT}(\ell)$ from $29 < \ell < 2509$ and the low-ℓ polarization data from $2 < \ell < 29$, which we denote as *Planck* (TT-lowP). The inclusion of the maps allows for stronger constraints on τ which in turn affects A_s, the primordial power spectrum amplitude. We have also chosen this configuration to allow us for an easy comparison with the DES-SV Cosmic Shear Cosmology paper (The Dark Energy Survey Collaboration et al. 2016a). The constraints from only using this configuration of *Planck* data when assuming a wCDM model are shown as the red contours in Fig. 5.

With the inclusion of the DES $\gamma_t(\theta)$ and $w(\theta)$ measurements, we were able to improve on the constraints on σ_8 and w from just *Planck* alone, which prefers $w \approx -1.5$ and $\sigma_8 \approx 1$. This is in part because DES provides modest constraints on H_0 which help break the degeneracy between h and Ω_m in the CMB. In addition, the *Planck* data set prefers higher values of σ_8 and h than the DES data, such that in combination, the two probes carve out a smaller area in parameter space. This produces strong constraints on w when the two data sets are combined. In combination with *Planck*, we find that $\Omega_m = 0.32 \pm 0.02$, $\sigma_8 = 0.88 \pm 0.03$ and $w = -1.15 \pm 0.09$.

Fig. 11 shows the result of combining our measurements with additional data sets beyond the CMB. The other probes that we consider are BAO measurements from 6dF (Beutler et al. 2011), BOSS (Anderson et al. 2014; Ross et al. 2015), Supernova Type Ia measurements (Betoule et al. 2014) and direct measurements of H_0 (Efstathiou 2014). These data sets alone give constraints of $\Omega_m = 0.33 \pm 0.02$ and $w = -1.07 \pm 0.06$ and no constraint on σ_8 (the posterior distribution on σ_8 is fully informed by the prior). Combining these data sets with DES and the CMB gives an improvement in precision and strengthens our results to $\Omega_m = 0.31 \pm 0.01$ and $\sigma_8 = 0.86 \pm 0.02$ and $w = -1.09 \pm 0.05$.

6.2 Comparison with DES cosmic shear

The Dark Energy Survey Collaboration et al. (2016a) measured the 2-point shear correlations, for the same DES-SV area and source catalogues. The best-fitting cosmological parameters in that work were $\sigma_8 = 0.81^{+0.16}_{-0.26}$ and $\Omega_m = 0.36^{+0.09}_{-0.21}$. Figs 4 and 5 show the constraints from the analysis presented in this work on those parameters together with constraints from the shear 2-point correlations for the

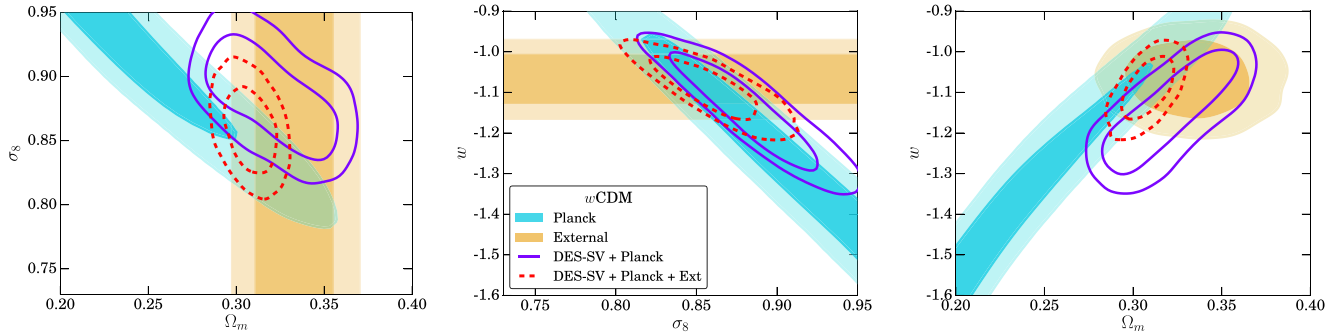

Figure 11. Constraints on σ_8, w and Ω_m using DES ($w(\theta)$ x $\gamma_t(\theta)$) in combination with *Planck* (solid purple) and DES in combination with *Planck* plus BAO, SN Ia and H_0 measurements (dashed red). Also shown are the constraints from *Planck* only (filled blue) and BAO, SN Ia and H_0 measurements only (filled yellow).

ΛCDM and *w*CDM models, respectively. There is very good agreement between the two analyses and a similar degeneracy direction in the Ω_m–σ_8 plane as well.

The shape of the contours for the two methods in Fig. 4 is somewhat different, with the cosmic shear contours being more elongated. We find that the slope α in the derived parameter $S_8 \equiv \sigma_8(\Omega_m/0.3)^\alpha$ is 0.16 for $w(\theta)$ and $\gamma_t(\theta)$ instead of 0.478 for cosmic shear. In part because the covariance between Ω_m and σ_8 is weaker, the constraints on each parameter are slightly stronger for the $w(\theta)$ and $\gamma_t(\theta)$ case. The results in this analysis are less sensitive to errors in the lensing shear and redshift distribution of source galaxies since these do not impact $w(\theta)$ at all, and additive errors in the shear cancel out of $\gamma_t(\theta)$ at lowest order. On the other hand, cosmic shear measurements are unaffected by errors in the galaxy biasing model and systematic errors in the measurement of galaxy clustering. Furthermore, the derived parameter S_8 is better constrained by DES cosmic shear. While there is significant complementarity in the two measurements, they are also correlated because of the shared source galaxies. The combination of all three 2-point functions taking into account covariances is an important next step in the cosmological analysis of DES.

Cosmic shear measurements obtained from the CFHTLenS (Heymans et al. 2013) constrain the combination of $S_8 = \sigma_8(\Omega_m/0.3)^\alpha$, where $\alpha = 0.46$, to be $S_8 = 0.774^{+0.032}_{-0.041}$ as their primary result. Again, the directionality of the parameter degeneracy between σ_8 and Ω_m is slightly stronger than for our joint probes analysis, but the results appear consistent.

6.3 Comparison with the literature

A number of previous papers have considered the combination of $w(\theta)$ and $\gamma_t(\theta)$ as probes of cosmology. Mandelbaum et al. (2013) perform an analysis with SDSS DR7 using the LRGs as the lenses and derive comparable constraints. With some cosmological parameters fixed, Mandelbaum et al. (2013) used a combination of three lensing and angular clustering measurements in the redshift range $0<z<0.5$ to obtain $\sigma_8 = 0.76 \pm 0.08$ and $\Omega_m = 0.27^{+0.04}_{-0.03}$. Several details of our analysis differ from Mandelbaum et al. (2013), but the broad approach of employing a quasi-linear analysis on large scales is similar and the results are consistent.

Cacciato et al. (2013) also measure the tangential shear and angular clustering from SDSS DR7 data, but differ in that they include small-scale clustering and consider a subset of the galaxy samples used by Mandelbaum et al. (2013). They adopt a halo-model approach which allows them to extend their analysis to much smaller scales than Mandelbaum et al. (2013), at the expense of requiring additional free parameters and model ingredients that are calibrated with simulations. With this small-scale approach, Cacciato et al. (2013) obtain $\Omega_m = 0.278^{+0.023}_{-0.026}$ and $\sigma_8 = 0.763^{+0.064}_{-0.049}$, again consistent with our derived constraints.

Similarly, More et al. (2015) use a halo model approach to calculate the joint likelihood using galaxy clustering, galaxy–galaxy lensing and galaxy abundance for the CMASS sample observed in BOSS using the CFHTLenS sources. They report that $\Omega_m = 0.31 \pm 0.02$ and $\sigma_8 = 0.79 \pm 0.04$. Applying an HOD model motivates the inclusion of small-scale information in their cosmology fits. In terms of number density and typical halo mass, the CMASS galaxies used by More et al. (2015) are closer to our redMaGiC sample than the LRGs in Mandelbaum et al. (2013), but they all derive consistent cosmological constraints.

7 CONCLUSIONS

In this paper, we have presented cosmological constraints from the combination of large-scale structure and weak gravitational lensing in the DES. Using a contiguous patch of 139 deg^2 from the SV period of observations, we have placed constraints on the matter density and the amplitude of fluctuations in the Universe as $\Omega_m = 0.31 \pm 0.09$ and $\sigma_8 = 0.74 \pm 0.13$, respectively. We also present joint constraints with CMB measurements from *Planck*, and additional low-redshift data sets. When allowing for a dark energy equation-of-state parameter w different to the ΛCDM value of -1, we find DES data improve the constraints on σ_8 as well as w. We leave a full tomographic analysis with multiple lens bins and a joint analysis with cosmic shear for future DES releases.

We have assessed the robustness of our results with respect to several variations in the choice of data vector, modelling and treatment of systematics. In particular, the results are stable under the use of two different shear catalogues, four different photo-z codes and two different estimators of the lensing signal. They also show consistency with the fiducial results when using a different lens bin, a different selection of angular scales or when adding a non-linear galaxy bias parameter.

The DES-SV region comprises only ∼3 per cent of the eventual survey coverage, and we expect to greatly improve on our constraining power with future data releases. For now, the analysis presented in this paper is complementary to and provides a useful consistency check with the analysis of the shear 2-point function presented in

The Dark Energy Survey Collaboration et al. (2016a). These analyses validate the robust modelling of systematic errors and galaxy bias, as well as the exhaustive testing of the shear pipeline, photo-z estimation and the redMaGiC galaxy sample selection in the DES.

ACKNOWLEDGEMENTS

We are grateful for the extraordinary contributions of our CTIO colleagues and the DECam Construction, Commissioning and SV teams in achieving the excellent instrument and telescope conditions that have made this work possible. The success of this project also relies critically on the expertise and dedication of the DES Data Management group.

Funding for the DES Projects has been provided by the US Department of Energy, the US National Science Foundation, the Ministry of Science and Education of Spain, the Science and Technology Facilities Council of the United Kingdom, the Higher Education Funding Council for England, the National Center for Supercomputing Applications at the University of Illinois at Urbana-Champaign, the Kavli Institute of Cosmological Physics at the University of Chicago, the Center for Cosmology and Astro-Particle Physics at the Ohio State University, the Center for Particle Cosmology and the Warren Center at the University of Pennsylvania, the Mitchell Institute for Fundamental Physics and Astronomy at Texas A&M University, Financiadora de Estudos e Projetos, Fundação Carlos Chagas Filho de Amparo à Pesquisa do Estado do Rio de Janeiro, Conselho Nacional de Desenvolvimento Científico e Tecnológico and the Ministério da Ciência e Tecnologia, the Deutsche Forschungsgemeinschaft and the Collaborating Institutions in the DES.

The DES data management system is supported by the National Science Foundation under Grant no. AST-1138766. The DES participants from Spanish institutions are partially supported by MINECO under grants AYA2012-39559, ESP2013-48274, FPA2013-47986, and Centro de Excelencia Severo Ochoa SEV-2012-0234, some of which include ERDF funds from the European Union.

The Collaborating Institutions are Argonne National Laboratory, the University of California at Santa Cruz, the University of Cambridge, Centro de Investigaciones Energeticas, Medioambientales y Tecnologicas-Madrid, the University of Chicago, University College London, the DES-Brazil Consortium, the Eidgenössische Technische Hochschule (ETH) Zürich, Fermi National Accelerator Laboratory, the University of Edinburgh, the University of Illinois at Urbana-Champaign, the Institut de Ciències de l'Espai (IEEC/CSIC), the Institut de Física d'Altes Energies, Lawrence Berkeley National Laboratory, the Ludwig-Maximilians Universität and the associated Excellence Cluster Universe, the University of Michigan, the National Optical Astronomy Observatory, the University of Nottingham, The Ohio State University, the University of Pennsylvania, the University of Portsmouth, SLAC National Accelerator Laboratory, Stanford University, the University of Sussex, and Texas A&M University.

REFERENCES

Anderson L. et al., 2014, MNRAS, 441, 24
Baldauf T., Smith R. E., Seljak U., Mandelbaum R., 2010, Phys. Rev. D, 81, 063531
Becker M. R. et al., 2016, Phys. Rev. D, 94, 022002
Behroozi P. S., Wechsler R. H., Wu H.-Y., 2013a, ApJ, 762, 109
Behroozi P. S., Wechsler R. H., Wu H.-Y., Busha M. T., Klypin A. A., Primack J. R., 2013b, ApJ, 763, 18
Betoule M. et al., 2014, A&A, 568, 22
Beutler F. et al., 2011, MNRAS, 416, 3017
Blanton M. R. et al., 2003, ApJ, 592, 819
Blazek J., McQuinn M., Seljak U., 2011, J. Cosmol. Astropart. Phys., 5, 1
Nakajima, RBlazek J., Mandelbaum R., Seljak U.2012, J. Cosmol. Astropart. Phys., 5, 41
Blazek J., Vlah Z., Seljak U., 2015, J. Cosmol. Astropart. Phys., 8, 15
Bonnett C. et al., 2016, Phys. Rev. D, 94, 042005
Brainerd T. G., Blandford R. D., Smail I., 1996, ApJ, 466, 623
Cacciato M., van den Bosch F. C., More S., Li R., Mo H. J., Yang X., 2009, MNRAS, 394, 929
Cacciato M., van den Bosch F. C., More S., Mo H., Yang X., 2013, MNRAS, 430, 767
Carrasco Kind M., Brunner R. J., 2013, MNRAS, 432, 1483
Catelan P., Kamionkowski M., Blandford R. D., 2001, MNRAS, 320, 7
Chang C. et al., 2015, Phys. Rev. Lett., 115, 1301
Clampitt J. et al., 2016, preprint (arXiv:1603.05790)
Crocce M. et al., 2016, MNRAS, 455, 4301
Cunha C. E., Huterer D., Busha M. T., Wechsler R. H., 2012, MNRAS, 423, 909
de Jong J. T. A., Verdoes Kleijn G. A., Kuijken K. H., Valentijn E. A., 2013, Exp. Astron., 35, 25
de Jong J. T. A. et al., 2015, A&A, 582, A62
Efstathiou G., 2014, MNRAS, 440, 1138
Erben T. et al., 2013, MNRAS, 433, 2545
Feroz F., Hobson M. P., Bridges M., 2009, MNRAS, 398, 1601
Flaugher B. et al., 2015, AJ, 150, 150
Friedrich O., Seitz S., Eifler T. F., Gruen D., 2016, MNRAS, 456, 2662
Giannantonio T. et al., 2016, MNRAS, 456, 3213
Gillis B. R. et al., 2013, MNRAS, 431, 1439
Górski K. M., Hivon E., Banday A. J., Wandelt B. D., Hansen F. K., Reinecke M., Bartelman M., 2005, ApJ, 622, 759
Graff P., Feroz F., Hobson M. P., Lasenby A., 2014, MNRAS, 441, 1741
Gruen D. et al., 2016, MNRAS, 455, 3367
Seljak, UGuzik J.2001, MNRAS, 321, 439
Hartlap J., Simon P., Schneider P., 2007, A&A, 464, 399
Heymans C. et al., 2012, MNRAS, 427, 146
Heymans C. et al., 2013, MNRAS, 432, 2433
Hirata C., Seljak U., 2004, Phys. Rev. D, 70, 063526
Howlett C., Lewis A., Hall A., Challinor A., 2012, J. Cosmol. Astropart. Phys., 4, 027
Hudson M. J. et al., 2015, MNRAS, 447, 298
Jarvis R. M., Bernstein G., Jain B., 2004, MNRAS, 352 338
Jarvis M. et al., 2016, MNRAS, 460 2245
Joachimi B. et al., 2015, Space Sci. Rev., 193, 1
Joachimi B., Mandelbaum R., Abdalla F. B., Bridle S. L., 2011, A&A, 527, 26
Kaiser N., 1992, ApJ, 388, 272,
Kuijken K. et al., 2015, MNRAS, 454, 3500
Landy S. D., Szalay A. S., 1993, ApJ, 412, 64
Lawrence E., Heitmann K., White M., Higdon D., Wagner C., Habib S., Williams B., 2010, ApJ, 713, 1322
Leauthaud A. et al., 2012, ApJ, 744, 159
Lehmann B. V., Mao Y.-Y., Becker M. R., Skillman S. W., Wechsler R. H., 2015, preprint (arXiv:1510.05651)
Leistedt B. et al., 2016, ApJS, 226, 24
Lewis A., Challinor A., Lasenby A., 2000, ApJ, 538, 473
Li T. S. et al., 2016, AJ, 151, 157
Limber D. N., 1953, ApJ, 117, 134
Mandelbaum R., Seljak U., Cool R. J., Blanton M., Hirata C. M., Brinkmann J., 2006, MNRAS, 372, 758
Mandelbaum R., Seljak U., Hirata C. M., 2008, J. Cosmol. Astropart. Phys., 8, 6
Mandelbaum R., Slosar A., Baldauf T., Seljak U., Hirata C. M., Nakajima R., Reyes R., Smith R. E., 2013, MNRAS, 432, 1544
Mao Y.-Y., Williamson M., Wechsler R. H., 2015, ApJ, 810, 21
Marian L., Smith R. E., Angulo R. E., 2015, MNRAS, 451, 1418

McCarthy I. G., Schaye J., Bower R. G., Ponman T. J., Booth C. M., Dalla Vecchia C., Springel V., 2011, MNRAS, 42, 1965
McDonald P., 2006, Phys. Rev. D, 74, 103512
Miyazaki S. et al., 2012, Proc. SPIE, 8446, 84460Z
Monet D. G. et al., 2003, AJ, 125, 984
More S., Miyatake H., Mandelbaum R., Takada M., Spergel D., Brownstein J., Schneider D. P., 2015, ApJ, 806, 2
Norberg P., Baugh C. M., Gaztañaga E., Croton D. J., 2009, MNRAS, 396, 19
Park Y. et al., 2016, Phys. Rev. D, 94, 063533
Planck Collaboration XIII 2016, A&A, 594, 13
Reddick R. M., Wechsler R. H., Tinker J. L., Behroozi P. S., 2013, ApJ, 771, 30
Ross A. J. et al., 2011, MNRAS, 417, 1350
Ross A. J. et al., 2012, MNRAS, 424, 564
Ross A. J. et al., 2014, MNRAS, 437, 1109
Ross A. J., Samushia L., Howlett C., Percival W. J., Burden A., Manera M., 2015, MNRAS, 449, 835
Rozo E., Rykoff E. S., Becker M., Reddick R. M., Wechsler R. H., 2015, MNRAS, 453, 38
Rozo E. et al., 2016, MNRAS, 461, 1431
Rykoff E. S. et al., 2014, ApJ, 785, 104
Sadeh I., Abdalla F. B., Lahav O., 2016, PASP, 128, 104502
Sánchez C. et al., 2014, MNRAS, 445, 1482
Seljak U., 2000, MNRAS, 318, 203
Sheldon E. S., 2014, MNRAS, 444, L25
Sheldon E. S. et al., 2004, AJ, 127, 2544
Sifón C. et al., 2015, MNRAS, 454, 3938
Singh S., Mandelbaum R., 2015, MNRAS, 450, 2195
Smith R. E. et al., 2003, MNRAS, 341, 1311
Springel V., 2005, MNRAS, 364, 1105
Suchyta E. et al., 2016, MNRAS, 457, 786
Takahashi R., Sato M., Nishimichi T., Taruya A., Oguri M., 2012, ApJ, 761, 152
The Dark Energy Survey Collaboration et al. 2016a, Phys. Rev. D, 94, 022001
The Dark Energy Survey Collaboration et al. 2016b, MNRAS, 460, 1270
Troxel M. A., Ishak M., 2015, Phys. Rep., 558, 1
Tyson J. A., Valdes F. J. F., Mills A. P., Jr1984, ApJ, 281, L59
van Daalen M. P., Schaye J., Booth C. M., Dall Vecchia C., 2011, MNRAS, 415, 3649
van Uitert E. et al., 2016, MNRAS, 459, 3251
Velander M. et al., 2014, MNRAS, 437, 2111
Vikram V. et al., 2015, Phys. Rev. D, 92, 022006
Viola M. et al., 2015, MNRAS, 452, 3529
Yang X., Mo H. J., van den Bosch F. C., Jing Y. P., Weinmann S. M., Meneghetti M., 2006, MNRAS, 373, 1159
Yoo J., Seljak U., 2012, Phys. Rev. D, 86, 083504
York D. G. et al., 2000, AJ, 120, 9
Zuntz J., Kacprzak T., Voigt L., Hirsch M., Rowe B., Bridle S., 2013, MNRAS, 434, 1604
Zuntz J. et al., 2015, Astron. Comput., 12, 45

APPENDIX A: EXCESS SURFACE DENSITY ΔΣ

In this section, we present complementary cosmology results obtained for the fiducial redMaGiC lens bin ($0.35 < z < 0.50$) by using the excess surface density, $\Delta\Sigma(R)$ as a proxy for the galaxy–galaxy lensing signal of redMaGiC galaxies. For this purpose, we define another lensing estimator that optimally weights each lens–source pair of galaxies depending on the line-of-sight distance separating them. This effectively downweights pairs of galaxies which are very close and for which we expect a small lensing efficiency. The observable is estimated from the measured shapes of background galaxies as

$$\Delta\Sigma^{\rm lens}(R; z_{\rm L}) = \frac{\sum_j \left[\omega'_j \gamma_{t,j}(R)/\Sigma^{-1}_{{\rm crit},j}(z_{\rm L}, z_{\rm s})\right]}{\sum_j \omega'_j}, \tag{A1}$$

where the summation $\sum_j$ goes over all the source galaxies in the radial bin R, around all the lens galaxy positions, and the weight factor for the jth galaxy is given by

$$\omega'_j = \omega_j \, \Sigma^{-2}_{{\rm crit},j}(z_{\rm L}, z_{\rm s}) \, . \tag{A2}$$

Note that, in contrast with $\gamma_{\rm t}(\theta)$, for $\Delta\Sigma$ we bin source galaxies according to radial distance R in the region around each lens galaxy, instead of angular scale θ. In order to estimate distances, we assume a flat ΛCDM model with $\Omega_{\rm m} = 0.3$. The weighting factor $\Sigma_{\rm crit}(z_{\rm L}, z_{\rm s})$ is computed as a function of lens and source redshifts for the assumed cosmology as

$$\Sigma_{\rm crit}(z_{\rm L}, z_{\rm s}) = \frac{c^2}{4\pi G} \frac{D_{\rm A}(z_{\rm s})}{D_{\rm A}(z_{\rm L}) D_{\rm A}(z_{\rm L}, z_{\rm s})}, \tag{A3}$$

where $\Sigma^{-1}_{\rm crit}(z_{\rm L}, z_{\rm s}) = 0$ for $z_{\rm s} < z_{\rm L}$ and $D_{\rm A}$ is the angular diameter distance. We have checked that changes in the assumed cosmology have little impact in the estimation of $\Delta\Sigma$ so that they are not relevant for the analysis presented in this work [see also Mandelbaum et al. (2013)]. Finally, just as we do with tangential shear measurements, our final estimator involves subtracting the contribution around random points, to which now we assign redshifts randomly drawn from the real lens redshift distribution.

Fig. A1 shows the clustering and the galaxy–galaxy lensing signals, the latter using the alternative $\Delta\Sigma$ estimator, both binned

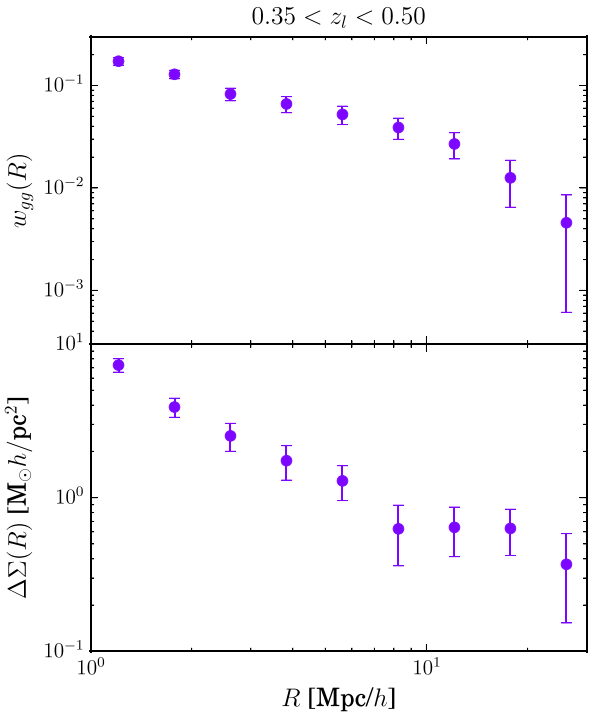

Figure A1. Same as our fiducial measurement plot in Fig. 2, but using the alternative lensing estimator $\Delta\Sigma$. In addition, the data are binned with respect to projected physical distance (R [Mpc h^{-1}]) rather than angle [θ (arcmin)]. The measurements are very similar to our fiducial results, as are the corresponding cosmological constraints in Fig. 6.

according to projected radial distance R around lenses. In this case, we use all source galaxies available in the NGMIX fiducial shear catalogue and we weight each lens–source galaxy pair according to their individual photometric redshifts so that nearby pairs for which we expect a small lensing efficiency are effectively downweighted. For the angular clustering, essentially the same data set is used in Fig. A1 as for our fiducial results pictured in Fig. 2. Thus, the two plots are very similar, with the main difference being the range of scales shown on the x-axis.

Our cosmological constraints obtained from fitting for $\Delta\Sigma(R)$ and $w(R)$ are shown in Fig. 6. These are consistent with our fiducial results, and show tighter constraints on parameters like $\Omega_{\rm m}$, due to the optimal lens weighting and the larger number of source galaxies effectively used. However, we do not use this estimator as the fiducial since we follow the photo-z error modelling of Bonnett et al. (2016) and The Dark Energy Survey Collaboration et al. (2016a), where the nuisance parameters act as an overall shift in the full-stacked distribution instead of on a galaxy-by-galaxy basis. Our choice of estimator does not seem to have a large impact on the constraints derived from our analysis (see Fig. 6).

APPENDIX B: NGMIX VERSUS IM3SHAPE

In Section 5.3, we studied the consistency of the obtained cosmological constraints when using the two shear pipelines presented in Jarvis et al. (2016). In Fig. B1, we show the actual comparison of the lensing measurements from the two shear pipelines, for all the different lens–source bin configurations. The IM3SHAPE results are an excellent match to our fiducial measurements with NGMIX (shown earlier in Fig. 2).

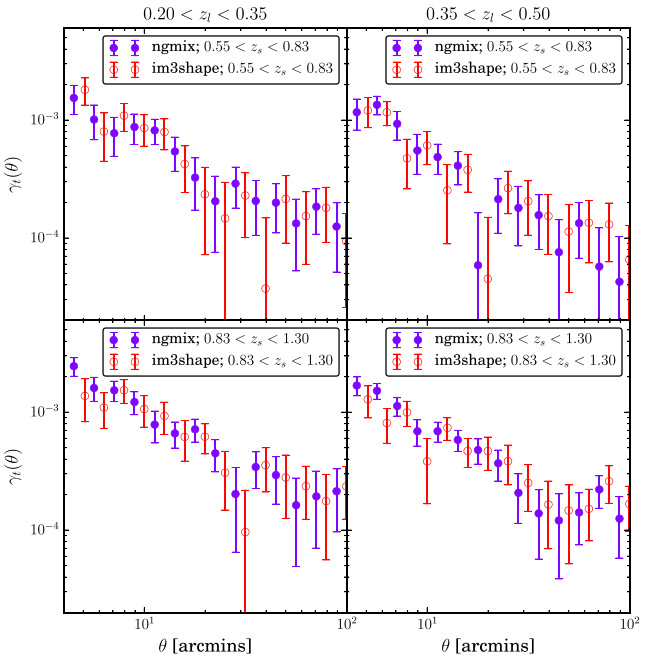

Figure B1. Comparison of the tangential shear signal using NGMIX (solid purple circles) and IM3SHAPE (open red circles) shear pipelines. The result is shown for the two-lens redshift bins (left- and right-hand columns) and the two source redshift bins (upper and lower rows) used in this work. For all bin combinations, the agreement between pipelines is excellent.

[1]*Department of Physics and Astronomy, University of Pennsylvania, Philadelphia, PA 19104, USA*
[2]*Institut de Física d'Altes Energies (IFAE), The Barcelona Institute of Science and Technology, Campus UAB, E-08193 Bellaterra, Barcelona, Spain*
[3]*Center for Cosmology and Astro-Particle Physics, The Ohio State University, Columbus, OH 43210, USA*
[4]*Institut de Ciències de l'Espai, IEEC-CSIC, Campus UAB, Carrer de Can Magrans, s/n, E-08193 Bellaterra, Barcelona, Spain*
[5]*Jodrell Bank Center for Astrophysics, School of Physics and Astronomy, University of Manchester, Oxford Road, Manchester M13 9PL, UK*
[6]*Department of Physics, ETH Zurich, Wolfgang-Pauli-Strasse 16, CH-8093 Zurich, Switzerland*
[7]*Department of Physics, Stanford University, 382 Via Pueblo Mall, Stanford, CA 94305, USA*
[8]*Kavli Institute for Particle Astrophysics and Cosmology, PO Box 2450, Stanford University, Stanford, CA 94305, USA*
[9]*Fermi National Accelerator Laboratory, PO Box 500, Batavia, IL 60510, USA*
[10]*Kavli Institute for Cosmological Physics, University of Chicago, Chicago, IL 60637, USA*
[11]*Department of Physics, University of Chicago, 5640 South Ellis Avenue, Chicago, IL 60637, USA*
[12]*Jet Propulsion Laboratory, California Institute of Technology, 4800 Oak Grove Dr., Pasadena, CA 91109, USA*
[13]*Institute of Astronomy, University of Cambridge, Madingley Road, Cambridge CB3 0HA, UK*
[14]*Kavli Institute for Cosmology, University of Cambridge, Madingley Road, Cambridge CB3 0HA, UK*
[15]*SLAC National Accelerator Laboratory, Menlo Park, CA 94025, USA*
[16]*Department of Physics, ETH Zurich, Wolfgang-Pauli-Strasse 16, CH-8093 Zurich, Switzerland*
[17]*Department of Physics and Astronomy, University College London, Gower Street, London WC1E 6BT, UK*
[18]*Institució Catalana de Recerca i Estudis Avançats, E-08010 Barcelona, Spain*
[19]*Department of Physics, University of Arizona, Tucson, AZ 85721, USA*
[20]*Brookhaven National Laboratory, Bldg 510, Upton, NY 11973, USA*
[21]*Cerro Tololo Inter-American Observatory, National Optical Astronomy Observatory, Casilla 603, La Serena, Chile*
[22]*Department of Physics and Electronics, Rhodes University, PO Box 94, Grahamstown 6140, South Africa*
[23]*CNRS, UMR 7095, Institut d'Astrophysique de Paris, F-75014 Paris, France*
[24]*Sorbonne Universités, UPMC Univ Paris 06, UMR 7095, Institut d'Astrophysique de Paris, F-75014 Paris, France*
[25]*Laboratório Interinstitucional de e-Astronomia - LIneA, Rua Gal. José Cristino 77, Rio de Janeiro RJ-20921-400, Brazil*
[26]*Observatório Nacional, Rua Gal. José Cristino 77, Rio de Janeiro RJ-20921-400, Brazil*
[27]*Department of Astronomy, University of Illinois, 1002 W. Green Street, Urbana, IL 61801, USA*
[28]*National Center for Supercomputing Applications, 1205 West Clark St., Urbana, IL 61801, USA*
[29]*Institute of Cosmology and Gravitation, University of Portsmouth, Portsmouth PO1 3FX, UK*
[30]*School of Physics and Astronomy, University of Southampton, Southampton SO17 1BJ, UK*
[31]*Excellence Cluster Universe, Boltzmannstr. 2, D-85748 Garching, Germany*
[32]*Faculty of Physics, Ludwig-Maximilians-Universität, Scheinerstr. 1, D-81679 Munich, Germany*
[33]*Department of Astronomy, University of Michigan, Ann Arbor, MI 48109, USA*
[34]*Department of Physics, University of Michigan, Ann Arbor, MI 48109, USA*
[35]*Department of Physics, The Ohio State University, Columbus, OH 43210, USA*
[36]*Australian Astronomical Observatory, North Ryde, NSW 2113, Australia*

[37] *Departamento de Física Matemática, Instituto de Física, Universidade de São Paulo, CP 66318, CEP 05314-970, São Paulo, SP, Brazil*
[38] *George P. and Cynthia Woods Mitchell Institute for Fundamental Physics and Astronomy, and Department of Physics and Astronomy, Texas A&M University, College Station, TX 77843, USA*
[39] *Department of Astronomy, The Ohio State University, Columbus, OH 43210, USA*
[40] *Department of Astrophysical Sciences, Princeton University, Peyton Hall, Princeton, NJ 08544, USA*
[41] *Max Planck Institute for Extraterrestrial Physics, Giessenbachstrasse, D-85748 Garching, Germany*
[42] *Department of Physics and Astronomy, Pevensey Building, University of Sussex, Brighton BN1 9QH, UK*
[43] *Centro de Investigaciones Energéticas, Medioambientales y Tecnológicas (CIEMAT), Madrid, Spain*
[44] *ICTP South American Institute for Fundamental Research Instituto de Física Teórica, Universidade Estadual Paulista, 01140-070 São Paulo, Brazil*
[45] *Computer Science and Mathematics Division, Oak Ridge National Laboratory, Oak Ridge, TN 37831*
[46] *Argonne National Laboratory, 9700 South Cass Avenue, Lemont, IL 60439, USA*

This paper has been typeset from a TEX/LATEX file prepared by the author.